8-2019

Fabrication of Polyvinylidene Fluoride Hollow Fiber Membranes for Membrane Distillation

Abdullah Al Balushi

Fabrication of Polyvinylidene Fluoride Hollow Fiber Membranes for Membrane

Distillation

by

Abdullah Al Balushi

A THESIS

Presented to the Faculty of

The Graduate College at the University of Nebraska

In Partial Fulfillment of Requirements

For the Degree of Master of Science

Major: Chemical Engineering

Under the Supervision of Professor Siamak Nejati

Lincoln, Nebraska

August 2019

Fabrication of Polyvinylidene Fluoride Hollow Fiber Membranes for Membrane

Distillation

Abdullah Al Balushi, M.S.

University of Nebraska, 2019

Advisor: Siamak Nejati

Desalination technologies can help humanity tap into the most abundant source of water on earth, seawater; however, desalination is an energy-demanding process. Most of the desalination plants worldwide use conventional energy resources; therefore, desalination leaves a large carbon footprint. Solar energy is an available source of energy that can be harvested and integrated into desalination systems.

Membrane distillation (MD) is an emerging purification technology that many offers many advantages over traditional desalination systems. For starters, it can utilize low-grade thermal energy to drive the separation, therefore, it can be suitably integrated into the solar-thermal energy scheme. Additionally, MD can be used to desalinate challenging water streams with minimal pretreatment, which makes it a suitable candidate for off-grid desalination in rural regions.

Herein, the lack of proper membranes and designed modules, membrane wetting and fouling, and the thermodynamic inefficiency in this system were identified as the bottleneck of the MD process, and novel solutions to tackle challenges were investigated. Polyvinylidene fluoride (PVDF) membranes suitable for MD were fabricated using nonsolvent induced phase separation (NIPS). The membranes were fully characterized to gain insight into the characteristics of MD membranes. By adjusting the parameters

controlling NIPS, membrane characteristics such as porosity, thickness, geometry, surface topography, and gas permeability were controlled. The desalination performance of the membranes, as well as their fouling and wetting propensity, were evaluated and studied. Some post-processing methods were employed on the membranes to hinder their fouling and wetting tendencies in MD operation. The membranes that were fabricated in this study displayed robust performance in challenging water streams.

Acknowledgements

Table of Contents

List of Figures

List of Tables

Chapter 1. Introduction

1.1 Background

The rapid increase in the world population is making water availability a major challenge for humanity. According to the UNESCO, three out of ten people do not have access to safe drinking water as of 2019 [1]. The World Health Organization estimates that 485,000 deaths each year are caused by contaminated water resources [2]. Despite improvements in water resource management, various regions around the world do not have sufficient amount of potable and freshwater.

Freshwater can be acquired from different resources such as groundwater, surface water, and seawater. It is estimated that the 97% of the water on earth is in the form of saline seawater, making it the most abundant source of water by a great margin [3]; thus, desalination of seawater must be given special attention. Additionally, some regions around the world are under such extreme water scarcity (including the Middle East and North Africa [4]) that seawater desalination is the most convenient source of water production. Nonetheless, water and energy production schemes are highly intertwined, which is often referred to as water-energy nexus. Therefore, increased water production at a lower energy cost is crucial to meet humanity's demands for freshwater.

Desalination technologies can be divided into two categories: thermal processes that require phase-change and membrane-based processes [5]. Examples of thermal desalination processes are (1) Multi-Stage Flash (MSF), (2) Multi-Effect Distillation (MED), (3) Thermal Vapor Compression (TVC), and (4) Mechanical Vapor Compression (MVC). Membrane-based technologies include Reverse Osmosis (RO), Forward Osmosis (FO), and Electrodialysis (ED). Among these technologies, RO has the highest energy

efficiency [6], which is why it accounts for ~84% of the total number of desalination plants worldwide [7].

> "If we could ever competitively--at a cheap rate--get freshwater from saltwater, ...(it) would be in the long-range interests of humanity as this could really dwarf any other scientific accomplishments."
>
> -- John F. Kennedy, 1962

1.2 Membrane Distillation

Membrane Distillation (MD) is a hybrid thermal and membrane-based desalination process in which water vapor diffuses through the pores of a porous hydrophobic film. The driving force is the vapor pressure gradient between the two interfaces of the membrane. In MD, water evaporates from the feed, diffused through the pores of the hydrophobic membrane, and condenses in the distillate side. MD offers ~100% theoretical rejection of nonvolatile components in the feed, such as dissolved solutes and oils.

There are four configurations for MD operation: direct contact membrane distillation (DCMD), air gap membrane distillation (AGMD), vacuum membrane distillation (VMD), and sweeping gas membrane distillation (SGMD). In DCMD operation, one side of the membrane is exposed to the heated saline feed and the other side is exposed to the cooled fresh distillate. In this configuration, the condensation occurs in the membrane module. The DCMD configuration is the most used configuration due to its simplicity. The caveat with the DCMD is the heat loss due to conduction through the membrane. In AGMD an air gap is placed between the membrane and a condensing surface. Water vapor passes through the gap and condenses on the surface. The benefit of

this configuration is the reduction of conductive heat losses. However, the addition of a stagnant fluid (air and water vapor) increases the mass transfer resistance, compromising the permeation of the vapor. Like DCMD, in AGMD the condensation takes place within the membrane module. In VMD, a vacuum is applied to the permeate side of the membrane module, and the permeated water is collected by using an external condenser. The heat loss by conduction is negligible. The driving force in VMD is the largest compared to other configurations. In SGMD, an inert gas flows in the permeate side of the membrane module collecting the diffused water vapor. Like VMD, SGMD requires an external condenser to collect the distilled water. The gas is not stagnant, therefore the mass transfer resistance is lower in the permeate site when it is compared with that of AGMD.

1.3   Motivation

Currently, the large-scale desalination plants use energy generated from fossil fuel; hence, the carbon footprint of these practices, considering the volume of water production, is large. The carbon footprint of RO desalination plants was estimated to be in the range of 0.4-6.7 kg CO_2eq/m^3 [8] and it is generally lower than the carbon footprint of thermal desalination plants [9]. Thermal desalination processes, such as MSF and MED, suffer from irreversible losses and often require greater energy input when they are compared with RO [10].

Solar energy is renewable and abundant. It can be harnessed using two main ways: converting sunlight to electricity using photovoltaic (PV) cells and converting sunlight to thermal energy using solar collectors. Recent reports on renewable energy technologies show promising progress in terms of energy efficiency and overall cost of power generation [11,12]. For instance, the levelized cost of electricity generation of concentrated solar

power (CSP) technology dropped from \$0.341 in 2010 to \$0.185 in 2018 [11]. Therefore, it is imperative to utilize solar energy to power desalination processes, ensuring a clean and sustainable approach for providing water supply.

MD is a promising candidate for solar desalination processes, and especially for off-grid processes. Figure 1.1 shows that MD has a significant potential to be coupled with solar energy compared with the conventional thermal desalination technologies, i.e., MED and MSF. Powering MED and MSF with solar energy has been challenging because they require a large and continuous supply of thermal energy [13]. On the contrary, MD can utilize low-grade thermal energy, therefore, using heat sources such as solar-thermal energy to drive the MD process is very appealing [14–19]. MD is reported to be more efficient than MED and MSF for the small-scale plants, and the energetic performance of MD has been shown to be superior for <1000 m^3 day^{-1} systems [20].
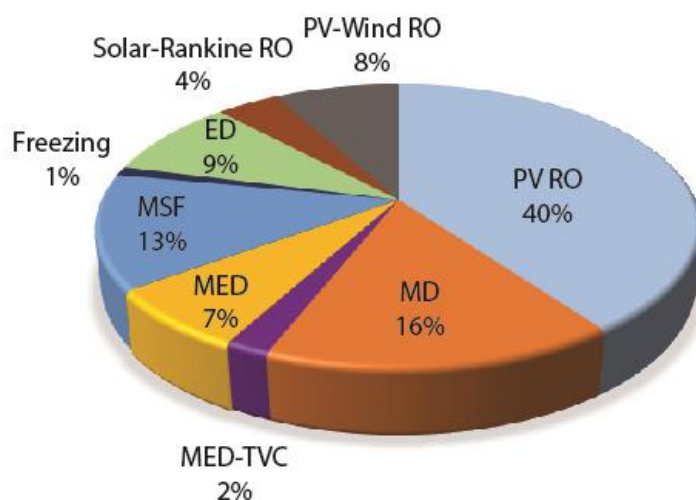
Figure 1.1 Share of desalination technologies in the pilot and commercial solar desalination plants installed worldwide [13].

Since MD requires phase change, it is inherently less energy efficient than RO [10]. For this reason, RO is the major contributor to solar desalination plants, as illustrated in Figure 1.1. (RO is typically operated with PV systems, rather than solar thermal collectors). MD is, however, still a promising candidate not only for desalination of saline water but also for the treatment of numerous challenging water resources where using RO would not be practical; examples of these water resources are oilfield-produced water [21], concentrated brines [22], textile wastewater [23], fermentation broth [24], and power plant blowout water [25], and among others [26]. Compared to RO, MD has a lower fouling propensity, higher salinity limit, higher water recovery, and less complex pretreatment requirement [20,27]. This makes MD a suitable candidate for off-grid solar-assisted desalination and water treatment.

1.4   Thesis Overview

In this thesis, the challenges that hinder the implementation of solar-assisted MD processes have been identified. Khayet found that the energy consumption and water production cost estimations of different MD systems were scattered [28]. This due to three main reasons: the lack of membranes and modules that are designed for MD, membrane wetting and fouling, and process inefficiencies [28,29]. In Chapter 2, the literature on MD membranes are reviewed and the challenges are identified. Polyvinylidene fluoride (PVDF) membranes are recognized as a great candidate for robust MD operation. PVDF membranes can be engineered through nonsolvent phase separation (NIPS). In Chapter 3, the methods to develop high performance and durable PVDF membranes for MD separation are described. Flat sheet and hollow fiber membranes are fabricated, characterized, and tested in MD. In Chapter 4, the results of membrane fabrication are

discussed, and the characteristics for durable MD operation are identified. Finally, in Chapter 5, the recommendation for the work required to further develop the MD process and integrate it with solar energy systems are provided.

Chapter 2.   Literature Review: Membranes for Membrane Distillation

2.1   Membrane Characteristics

Membranes for membrane distillation (MD) must be porous and hydrophobic. The typical pore size used in MD membranes ranges between 10 nm to 1 μm. Membranes with larger pore size have higher water flux due to reduced mass transfer limitation in the pores of the membrane; however, larger pore size leads to liquid penetrating the pores of the membranes according to the Young-Laplace equation (Eq. (3.3)). The porosity of the membrane should be as high as possible, so long as the membrane retains its mechanical integrity. The membrane must have low thermal conductivity to minimize heat losses by conduction through the membrane [30].

2.2   Challenges with MD Membranes

Recently, researchers have been developing polyvinylidene fluoride (PVDF) membranes with unique properties, such as larger pore size [31] and lower thickness [32], and dual-layer hydrophobic/hydrophilic membranes [33,34] to enhance the flux. However, they fail to address the challenges that face MD, such as wetting and fouling. Furthermore, the commercial membranes that have been used for MD were reported to fail when they were exposed to challenging water resources [21,25,35–37].

Gryta found that capillary polypropylene (PP) hollow fibers wetted when they were challenged with the fermentation broth due to organic compounds adsorbing to the membrane surface [24]. Commercial polytetrafluoroethylene (PTFE) membranes started wetting when challenged with 0.1 mM sodium dodecyl sulfate (SDS) surfactant [35], commercial flat sheet PVDF membranes wetted with 0.05 mM SDS [21], and commercial hollow fiber PVDF wetted with 0.15 mM SDS [38]. The presence of these organic

15

molecules in water induces their adsorption on the membrane surface and decreases the surface tension of water, and thus water starts to penetrate the pores.

Wetting in MD can be distinguished by four degrees: (1) no-wetting, (2) surface wetting, (3) partial wetting, and (4) full wetting, as illustrated in Figure 2.1 [39,40]. Surface wetting occurs when a layer of liquid water penetrates the membrane pores; however, the membrane maintains a gaseous interface and does not allow for liquid to wick through. The permeate flux may decline gradually as a result of the decrease in the interfacial temperature gradient (temperature polarization [41]); however, the salt rejection remains ~100%, because liquid cross over does not take place. The salt rejection starts to decline when partial wetting phenomenon begins: when some water starts to leak into the distillate side through the larger pores. Depending on the nature of pore wetting and the number of pores wetted, the permeate flux either keeps on falling or increases rapidly. Finally, in full wetting, the membrane no longer acts as a liquid/gas barrier, which results in the viscous flow of liquid water through the pores and a sharp decline in salt rejection.
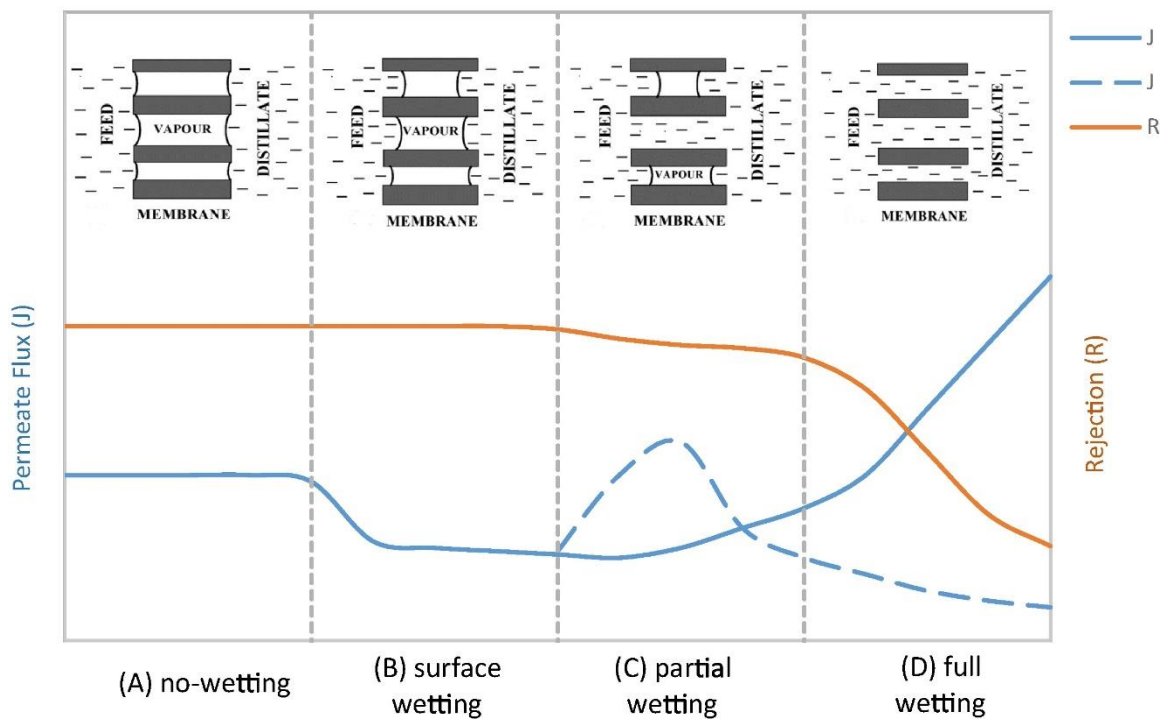
Figure 2.1 Membrane wetting degrees in membrane distillation [40].

Another challenge facing MD is membrane fouling. Membrane fouling in MD leads to the decline in membrane flux due to the blocking of membrane pores by foulants. The most common types of fouling in MD are inorganic scaling, organic fouling, and biofouling [42]. Fouling leads to wetting and decline in salt rejection in MD [37,40,42]. Several researchers reported the failure of commercial membranes when they were tested with water streams that were contaminated oil [21,38,43–49]. Others found that the membranes were susceptible to gypsum ($CaSO_4 \cdot 2H_2O$) and calcite ($CaCO_3$) scaling [25,36,37,50], and biofilms growth on the membrane surface [51,52].

To address these challenges, researchers have developed strategies and methods to modify the membrane's surface. Some researchers made hydrophilic modification on the membrane surface to create an underwater-oleophobic membrane for anti-oil-fouling

properties [43,45–47,53]. The hydrophilic surface creates a hydration layer on the membrane surface that repels the oil droplets. Other researchers produced superhydrophobic membranes by creating reentrant structures and introducing low surface energy materials on the surface [21,35,47,54–58]. These surfaces have been found by several researchers to effectively mitigate organic and inorganic fouling [25,59–69]. In most of these studies, the modification is performed on a commercial flat sheet membrane samples. There is a lack of research that modifies hollow fiber membranes for robust MD operation in challenging water resources. These modifications ought to be employed on hollow fiber membranes because they are crucial to the development of MD technology.

2.3 Commercial Membranes

PP, PTFE, and PVDF are the three most commonly used polymers for the fabrication of MD membranes. Membranes made of these polymers are commercially available and many reports on their performance in the MD process is summarized in literature [30,70]. However, the commercially available membranes used for MD are usually designed for other separation technologies, such as microfiltration; consequently, they do not offer the desired performance in MD [71]. As a result, the research focused on the fabrication of membranes and module designed for the MD application is still an ongoing topic.

Thomas et al. [29] reviewed the membrane materials that are used in MD studies. They found that PP membranes were the main choice for membranes in the early stage of research in MD process; however, the use of PP faded away due to the focus on other polymers such as PVDF. PVDF is an exceptional choice for MD because it can be processed using solution-based preparation methods in roll-to-roll schemes. Additionally,

PVDF is thermally, mechanically, and chemically stable, and it can be chemically modified using facile surface functionalization techniques [72]. Although flat sheet PVDF membranes are commercially available, hollow fiber membranes made of PVDF are not as readily available. Thus, the development of hollow fiber PVDF membranes for MD is of interest for researchers.

2.4 Nonsolvent Induced Phase Separation

Many researchers were able to fabricate high-performance PVDF membranes for MD with phase separation methods [32,33,73–76]. Phase separation techniques are simple processing techniques compared to mechanical extrusion, which is the technique used to prepare PTFE membranes [76]. Phase separation techniques can be achieved in roll-to-roll processes that are convenient for mass production of membranes. There are four main types of phase separation techniques: (1) nonsolvent induced phase separation (NIPS), (2) thermally induced phase separation (TIPS), (3) vapor induced phase separation, and (4) solvent evaporation [77]. Among the four processes, NIPS is the most common technique for the fabrication of PVDF membranes. Most of the research and development addressing fabrication of hollow fiber PVDF membranes for MD applications utilize NIPS.

In NIPS, the structure and morphology of the membrane can be explained by the thermodynamics and kinetics of the phase separation. The thermodynamics can be analyzed by the ternary phase diagram, as illustrated in Figure 2.2. For NIPS, there are two regions of interest in the diagram: the one-phase region, where the mixture is homogeneous, and the two-phase region, where the system separates into a polymer-rich (solid) and polymer-poor (liquid) phase [77,78]. The single-phase and two-phase regions exist on the left side and right side of the binodal curve (illustrated Figure 2.2), respectively.

In NIPS, after the polymer solution film is placed in the coagulation bath, the liquid-liquid demixing can take two pathways. The demixing occurs instantaneously, as demonstrated in Figure 2.2a, or delayed, as demonstrated in Figure 2.2b. In instantaneous demixing, the solution interface of the cast film (Point T) crosses the binodal curve and the demixing starts immediately. On the other hand, in delayed demixing, the process trajectory does not pass the binodal curve and the whole film can be assumed to be in the one-phase region until the composition reaches point T. Instantaneous demixing produce membranes with a dense skin layer and finger-like macrovoids [68] and delayed demixing produces a porous outer surface and sponge-like macroporous domain which are desired for MD applications [31,32,76,79,80]. (Note that the difference between instantaneous and delayed demixing is comparative and there is no definitive timeframe to distinguish the two [81]). Therefore, to control the kinetics and the trajectory of the phase inversion and achieve desired structural parameters for the membranes processed through NIPS, searching the space of parameter is of prime interest.
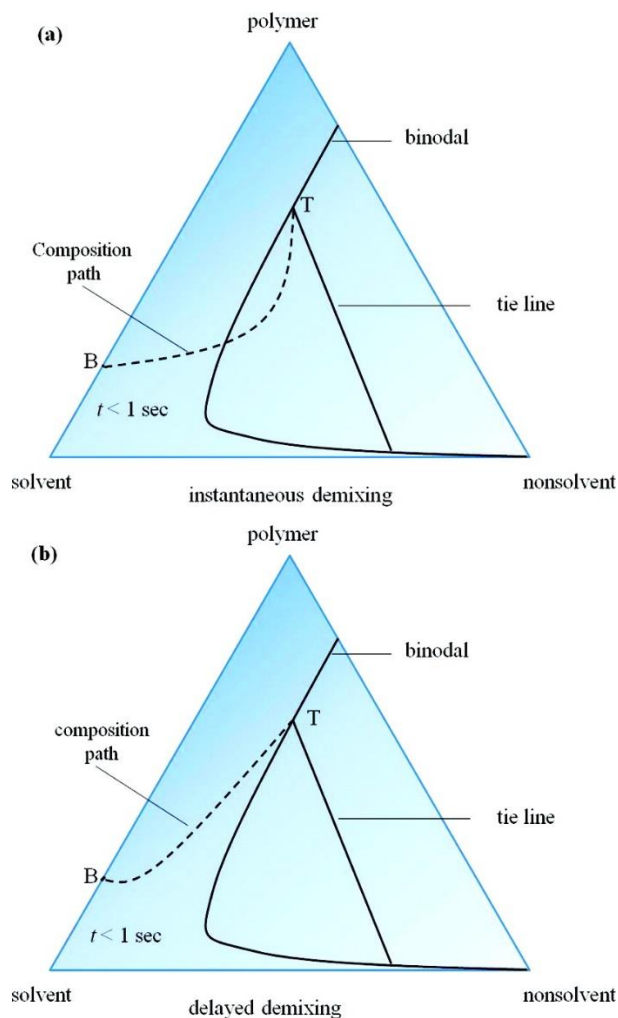
Figure 2.2 Composition path of cast film after of immersion in the nonsolvent. (a) Demonstrates instantaneous demixing and (b) demonstrates delayed demixing. Points B and T represent the bottom and the top of the cast film, respectively [78].

2.4.1   Effect of Solvent

Conventionally, dimethylformamide (DMF), N, N-dimethylacetamide (DMA), and N-methyl-2- pyrrolidone (NMP) are used as solvents for PVDF membrane fabrication. These solvents are toxic; therefore, using green alternatives to prepare membranes with desired properties is of interest [82]. Triethyl phosphate (TEP) is a nonconventional green solvent that has been recently used to fabricate PVDF membranes for MD [76,80].

The effect of solvent can be discussed by analyzing the solubility parameters of the polymer/solvent mixture, which can be broken into three components: the dispersion parameter (δ_d), the polar parameter (δ_p), and the hydrogen bonding parameter (δ_h). The total solubility parameter (δ) is equal to [78]:

$$\delta = \sqrt{\delta_d^2 + \delta_p^2 + \delta_h^2} \tag{2.1}$$

To understand the interactions between the polymer and the solvent, Hansen and Skaarup established the solubility parameter distance, Ra, which is a measure of the affinity between the solvent (1) and the polymer (2) [78] and can be calculated using Eq. (2.2):

$$Ra = \sqrt{4\left(\delta_{d2} - \delta_{d1}\right)^2 + \left(\delta_{p2} - \delta_{p1}\right)^2 + \left(\delta_{h2} - \delta_{h1}\right)^2} \tag{2.2}$$

The relative energy difference (RED) between the polymer and the solvent, which is a parameter that described the interaction between the polymer and the solvent, is equal to the ratio between Ra and the radius of the interaction of the Hansen solubility parameter (R_o) of the polymer [78]. A RED value lower than 1 indicates that the solubility has been met and the polymer is miscible in the solvent. On the other hand, a RED value greater than 1 indicates that the polymer is immiscible in the liquid, and the liquid is considered a nonsolvent. For a wide variety of solvents and polymers, the solubility parameters, as well as R_o, are tabulated by Hansen [83] and Table 2.1 presents the solubility parameters for PVDF, DMF, DMA, NMP, TEP, water, and isopropyl alcohol (IPA). The RED is calculated for each solvent with respect to its interaction with PVDF.

Table 2.1 Solubility parameters of different components [76,78,83]

Component	Dispersion[a]	Polar[a]	Hydrogen[a]	Total[a]	R_o[a]	Ra[a]	RED
PVDF	17	12.1	10.2	23.2	4.1		
DMF	17.4	13.7	11.2	24.8		2	0.5
DMA	16.8	11.5	10.2	22.8		0.7	0.2
NMP	18	12.3	7.2	23		3.6	0.9
TEP	16.8	11.5	9.2	22.3		1.4	0.3
Water	15.5	16	42.3	47.8		32.5	7.9
IPA	15.8	6.1	16.4	23.6		9	2.2

a: The unit for the solubility parameters is $(MPa)^{1/2}$

The Gibbs free energy of mixing, ΔG_m, for a polymeric solution was developed by Flory and Huggins [78,84]:

$$\Delta G_m = RT \left(n_1 \ln \phi_1 + n_2 \ln \phi_2 + \chi_{12} n_1 \ln \phi_2 \right) \tag{2.3}$$

where R is the ideal gas constant, T is the absolute temperature, n_1 and n_2 are the numbers of molecules of solvent (1) and polymer (2), ϕ is the volume fraction, and χ_{12} is the Flory interaction parameter, which is a characterization of the polymer-solvent interaction energy. χ_{12} can be determined experimentally or can be estimated using Eq. (2.4) [78]:

$$\chi_{12} = \frac{v_1}{RT} \left(\delta_1 - \delta_2 \right)^2 \tag{2.4}$$

where v_1 is the solvent's molar volume and R is the ideal gas constant. This model assumes that the polymer and solvent occupy lattice points and that the polymer behaves like a flexible chain as if it consists of a number of segments with the same size [78,84]. Several

modifications of this model have been made to account for the concentration dependence of the polymer-solvent interaction parameter χ_{12} [78,85].

2.4.2 Effect of Polymer

2.4.2.1 Concentration

Polymer concentration defines the final structure of the membrane. Higher polymer concentration solution yields less porous membranes. This is because the polymer concentration determines the volume fraction that the polymer occupies in cast film. Changing the polymer concentration has been shown to influence the pathway of precipitation as well; distinct structures can be obtained by changing the polymer concentration depending on the precipitation pathway as observed by Strathmann et al. [68,86].

2.4.2.2 Molecular Weight

The molecular weight of the polymer affects the viscosity and stability of the polymer solution. High polymer solution viscosity delays the diffusion of nonsolvent into the film, which leads to sponge-like structures [79,87]. Also, the molecular weight alters the volume fraction, ϕ, consequentially changing the Gibbs free energy of mixing.

2.4.3 Effect of Nonsolvent Composition

The composition of the nonsolvent plays a role in the precipitation process. The miscibility between the solvent and nonsolvent and the affinity between the polymer and the nonsolvent influence the final structure of the membrane. Water is the most commonly used nonsolvent, but alcohols, alcohol/water, and solvent/water mixtures have been used as coagulation media in NIPS [77]. Comparing the RED between water and PVDF (7.9)

and IPA and PVDF (2.2) (see Table 2.1), it is clear that the affinity between water and PVDF is weaker than that of IPA and PVDF. Using water as a nonsolvent induces instantaneous demixing that yields finger-like macrovoids with a dense skin layer. The addition of solvents and alcohols to the coagulation bath lowers the activity of nonsolvent and diffusion rates into the polymer, which delays the demixing.

Chapter 3.   Fabrication of Porous Membranes from PVDF

3.1   Introduction to Membrane Fabrication using NIPS

To fabricate flat sheet PVDF membranes using nonsolvent induced phase separation (NIPS), a film of the polymer solution can be cast on a substrate (Figure 3.1a) and immersed into the coagulation bath (Figure 3.1b) where the solvent-nonsolvent exchange occurs (Figure 3.1c). Similarly, hollow fiber membranes can be fabricated using the dry-jet wet spinning method described in the literature [88]. The polymer solution is extruded from the outer channel of a spinneret and a bore liquid flows in the inner tube of the spinneret, as illustrated in Figure 3.1d. The ejected streams from the spinneret flow into the coagulation bath (Figure 3.1e) and the solvent-nonsolvent exchange occurs in two interfaces, as illustrated in Figure 3.1f: between the bore fluid and the polymer solution and between the coagulation bath and the polymer solution.

The separation performance of membrane distillation (MD) is related to the morphology of the membrane. There are several characterization tools that can be used to obtain insight into the performance of the membranes. Electron microscopy offers direct visualization of the membrane morphology. Chemical spectroscopy analyzes the chemistry of the material. Porosity, pore size, and the gas permeation test are related to permeate flux in MD. The contact angle and surface pore size are related to the wettability of the membranes [30].
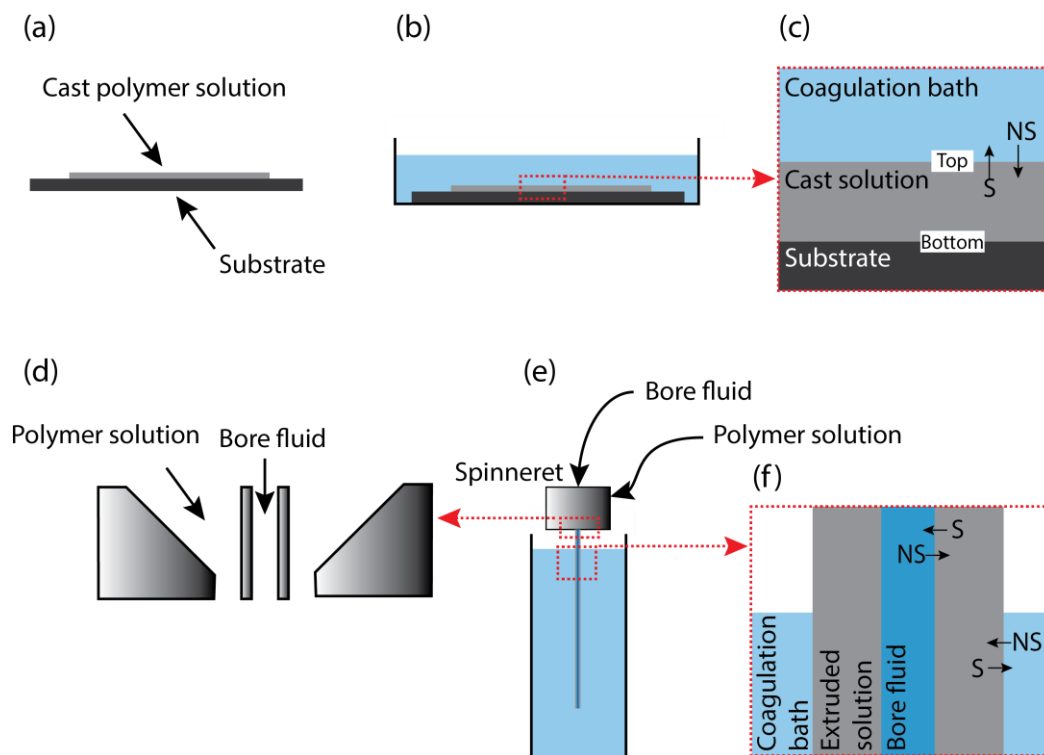
Figure 3.1 Schematic illustration of flat sheet and hollow fiber membrane fabrication using NIPS.

3.2 Materials and Chemicals

Polyvinylidene fluoride (PVDF, Kynar® HSV 900) was supplied by Arkema Inc., USA. Triethyl phosphate (TEP, 99.8%), perfluorobutanesulfonyl fluoride (PBSF, 96%), sodium dodecyl sulfate (SDS, 99%), calcium chloride (CaCl$_2$, anhydrous), sodium sulfate (Na$_2$SO$_4$), and PVDF (M$_W$= 530 kDa, 275 kDa) were purchased from Sigma-Aldrich. Ethanol (99.5%), isopropyl alcohol (IPA, ACS grade), sodium chloride (NaCl, ACS grade), and potassium hydroxide (KOH, ACE grade) were purchased from Fisher Scientific. Ethylene glycol (99.5%) was purchased from ACROS Organics. Hexafluoropropylene oxide (HFPO) was purchased from Oakwood Products. 1H,1H,2H,2H-perfluorodecyl acrylate (PFDA, 97%) was obtained from Frontier Scientific. Porefil® was purchased from Porometer, Belgium. Canola oil was purchased

from Wessel Oil. Deionized (DI) water was obtained from a Simplicity Ultrapure water purification system (Millipore, Billerica, MA). Ultrapure nitrogen was purchased from Matheson Gas Company.

3.3 Flat Sheet Membrane Fabrication

The polymer solution was prepared by dissolving 12 wt % PVDF (530 kDa) pellets in TEP. The solution was stirred overnight at 125 °C and 400 rpm. After the polymer was fully dissolved, the solution was left to rest at room temperature for 6 h to cool and degas. Then, using a casting knife (Gardco), the solution was cast on a glass plate (Figure 3.1a) at a speed of approximately 5 cm/s (room temperature; relative humidity ∼52%). The membrane thickness was adjusted by changing the gate height of the casting knife. After casting, the glass plate was submerged in a nonsolvent (coagulation bath) within 5 seconds to induce the phase separation (Figure 3.1b and c). The coagulation bath was prepared by mixing IPA and DI water at different volume ratios; the volumetric fraction of IPA in the coagulation bath was varied from 30 to 70 v/v %. After casting, the membranes were left in the coagulation bath for 5 min and then transferred to a pure DI water bath to remove the residual solvent. After complete solvent removal, the membranes were rinsed with ethanol and then dried for 12 h in a temperature-controlled oven (Quincy Lab, 20 GC) set at 75 °C.

3.4 Hollow Fiber Membrane Fabrication

Kynar® HSV 900 grade PVDF powder was dried in the vacuum oven at 50 ˚C before preparing the dope. The dope solution was prepared by dissolving the powder in TEP with a concentration of 12 wt. %. The mixture was stirred on a hot plate and the

temperature was set to 150 ˚C for 12 h. After the polymer fully dissolved, it was left to cool for 4 h and then transferred to a stainless steel syringe and left to degas.

The hollow fiber membranes were fabricated using a dry-jet wet spinning method at a 20 ˚C room temperature and 49-52% relative humidity. The dope and bore were fed to the spinneret (DeltaE Srl, Italy) using high-pressure syringe pumps (Fusion 6000, Chemyx, Inc., USA). NIPS occurred in a 1 L graduated cylinder filled with the coagulation bath (Figure 3.1e). The nascent fibers were left in the coagulation bath for 10 min and then transferred to a water bath. The water bath was changed after 24 h and exchanged with IPA after 48 h. The fibers were left in the IPA bath for another 24 h to remove excess TEP inside the pores of the fibers. Finally, the hollow fiber membranes were taped on a glass substrate and dried in the vacuum oven at 50 ˚C for 24 h. Table 3.1 lists the parameters used for spinning of membrane solutions. The parameters were adopted from previous studies [76], with modifications to fit the experimental setup.

Table 3.1 Spinning conditions for hollow fiber membrane fabrication.

Parameter	Value
Dope composition	12 wt. % PVDF/TEP
Dope flow rate	2.5 mL min^{-1}
Bore composition	20 v/v % TEP/water
Bore flow rate	1.5 mL min^{-1}
Coagulation bath	30 v/v % TEP/water
Air gap distance	3 cm

3.5   Post-Processing

3.5.1   Superhydrophobic Coating

The hollow fiber membranes were coated with polytetrafluoroethylene (PTFE) and low surface energy polymer poly (1H,1H,2H,2H-perfluorodecyl acrylate) (pPFDA) using a custom-built initiated chemical vapor deposition (iCVD) reactor [89]. The polymerization of PFDA monomer was achieved by using perfluorobutanesulfonyl fluoride (PBSF) as an initiator.

3.5.2   Hydrophilic Treatment

The hollow fiber membranes were treated using a facile chemical treatment procedure that was developed for flat sheet PVDF membranes and reported in [53]. In a typical procedure, a bundle hollow fiber membranes were immersed in 8 M KOH solution for 15 h with stirring. After the reaction, the membranes were washed for 40 min with DI water to remove excess KOH from the membrane surface and dried in the oven.

3.6   Membrane Characterization

3.6.1   Scanning Electron Microscopy

The scanning electron microscopy (SEM) data were collected using an FEI Helios NanoLab 660 microscope. The images of the cross-sections were acquired by fracturing the membranes in liquid nitrogen. The fractured membranes were dried in the vacuum oven for 4 h at 50 ˚C. Before taking the images, the membrane samples were coated with ~60 nm of gold using a Ted Pella sputtering machine (108 Auto).

3.6.2 Vibrational Spectroscopy

Fourier-transform infrared spectroscopy (FTIR) measurements were performed using the attenuated total reflection (ATR) module of Bruker Alpha-P. A small piece of hollow fiber sample was cut and placed on the diamond crystal of the ATR module. The FTIR measurements were performed using 24 high-resolution scans on each sample with a resolution of 4 cm^{-1}.

3.6.3 Porosity Measurement

The porosity of the flat sheet membranes was measured by comparing the weight of a dry and IPA-wet membrane sample. The porosity is estimated using Eq. (3.1):

$$\varepsilon = \frac{V_{pore}}{V_{membrane}} = \frac{\dfrac{m_{IPA}}{\rho_{IPA}}}{V_{pore} + V_{polymer}} = \frac{\dfrac{m_{IPA}}{\rho_{IPA}}}{\dfrac{m_{IPA}}{\rho_{IPA}} + \dfrac{m_{polymer}}{\rho_{polymer}}} \tag{3.1}$$

where ε, V, m, and ρ are the porosity, volume, mass, and density, respectively. The densities of IPA and PVDF were taken to be 0.786 g cm^{-3} and 1.78 g cm^{-3}, respectively. The porosity of the hollow fiber membranes was estimated by measuring the dry weight of a hollow fiber membrane sample. Knowing the length and the inner and outer diameter of the fibers from the SEM images, the volume of the fiber was estimated. The porosity is estimated by using Eq. (3.2):

$$\varepsilon = \frac{V_{pore}}{V_{membrane}} = \frac{V_{membrane} - V_{polymer}}{V_{membrane}} = 1 - \frac{m/\rho_{polymer}}{V_{membrane}} \tag{3.2}$$

3.6.4   Pore Size Distribution

The pore size distribution for the flat sheet membranes was evaluated by a wet/dry flow method using a custom-made gas permeation set-up. A commercial wetting liquid, Porefil®, with low surface tension (16 mN m^{-1}) and vapor pressure (399 Pa at 298 K) was used to wet the membranes. The membranes were immersed in the wetting liquid for a minute and then placed inside the filter holder. The holder was connected to the gas permeation setup illustrated in Figure 3.2. The pore size distribution was performed using the pressure step/stability method [90], where the upstream pressure was increased only when the flow rate stabilized indicating that all the pores of the same size were emptied. The pressure was increased with the increment of ~8 kPa until all the pores were emptied and the wet curve was obtained. The dry curves were obtained by sweeping the pressure and measuring the flow of the dry membrane. The pore size is related to the differential pressure and surface tension of the liquid, according to the Young-Laplace equation [91] presented in Eq. (3.3):

$$LEP = \frac{4\gamma \cos\theta}{d_p} \qquad\qquad (3.3)$$

where *LEP* is the liquid entry pressure, γ is the surface tension of the liquid, θ is the contact angle, and d_p is the pore size (diameter). The pore size distribution analysis was performed on the dry and wet curves by using a method described in the literature [30]. The contact angle of Porefil® on the membrane was assumed to be zero. Additionally, the pore size of the hollow fiber membranes was analyzed using image analysis software (ImageJ).

3.6.5   Gas Permeation

The gas permeation tests were performed using a custom-built gas permeation setup as illustrated in Figure 3.2. Ultrapure nitrogen was used as the gas. The pressure of nitrogen gas in the upstream was controlled using a digital pressure regulator (ControlAir Inc., T900X). The flow rate of the gas was measured using a digital mass flow meter (Omega Engineering, 0-10 L min^{-1}, FMA1720), the pressure of the gas in the upstream was measured using a digital pressure transducer (Honeywell, 0-100 psi, px2an1xx100psaax), and the pressure of the gas in the downstream was assumed to be atmospheric. For flat sheet membranes, we punched the membranes to 13 mm diameter circles and inserted them into a stainless-steel filter holder (13 mm, Advantec) with an effective area of 0.9 cm^2. For the hollow fiber membranes, we potted the fibers inside a 9 cm long stainless-steel nipple and applied the nitrogen gas to the lumen of the fiber. The effective length of the fibers inside the housing was 7 cm.
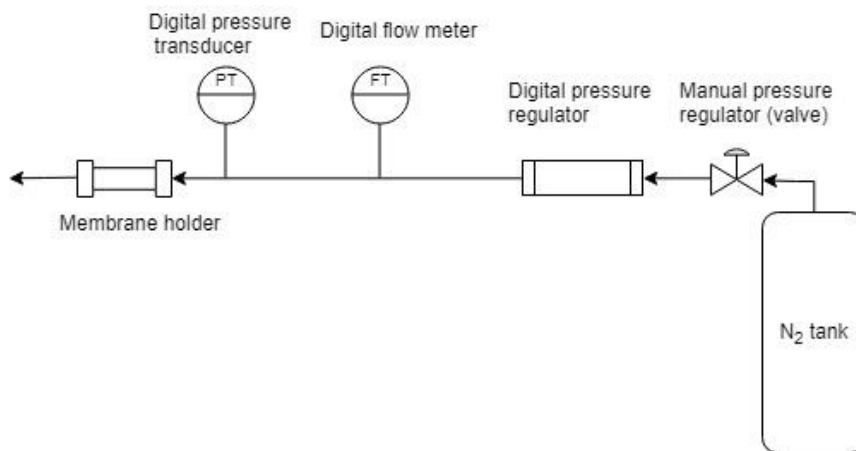
Figure 3.2 Schematic of the gas permeation setup.

The flux of gas can be described using Eq. (3.3):

$$J_g = B_g \Delta P \tag{3.4}$$

where J_g is the flux of the gas, B_g is the permeability of the gas, and ΔP is the differential pressure. The value of B_g is obtained by linearly fitting the gas permeation data to Eq. (3.4).

3.6.6   Contact Angle and Wettability

The water contact angle on the membrane surfaces was measured using an optical tensiometer (Rame-Hart, model 590) and the sessile drop method. A 5 µL DI water droplet was placed on the dried membrane sample. To test the wettability of the hollow fiber membranes, we immersed them in water, ethylene glycol, canola oil, and ethanol. When wetting occurs, the liquid rises due to capillarity action; however, in nonwetting condition, the liquid surface bends downwards. We captured the images using a high magnification camera (Opti-tekscope). The contact angle was measured using image analysis.

3.7   Hollow Fiber Membrane Packing

The hollow fiber membranes were fabricated according to the procedure illustrated in Figure 3.3. The spacers, illustrated in Figure A.1 and Figure A.2 in Appendix A, were printed with a Form 2 3D printer (FormLabs, Massachusetts, USA) using clear acrylic resin. First, two 3D printed spacers were placed together, and the fibers were passed through their holes. The fibers were potted from one side with epoxy and left to cure. Then the second spacer was inserted into a polypropylene tubing (9.525 mm inner diameter) followed by the hollow fibers. The spacers were both sealed to the tubing and the hollow fibers were potted to the spacers. The module was relaxed for 24 h for the epoxy to cure before starting the experiment. The length of the tested modules was 10 cm.
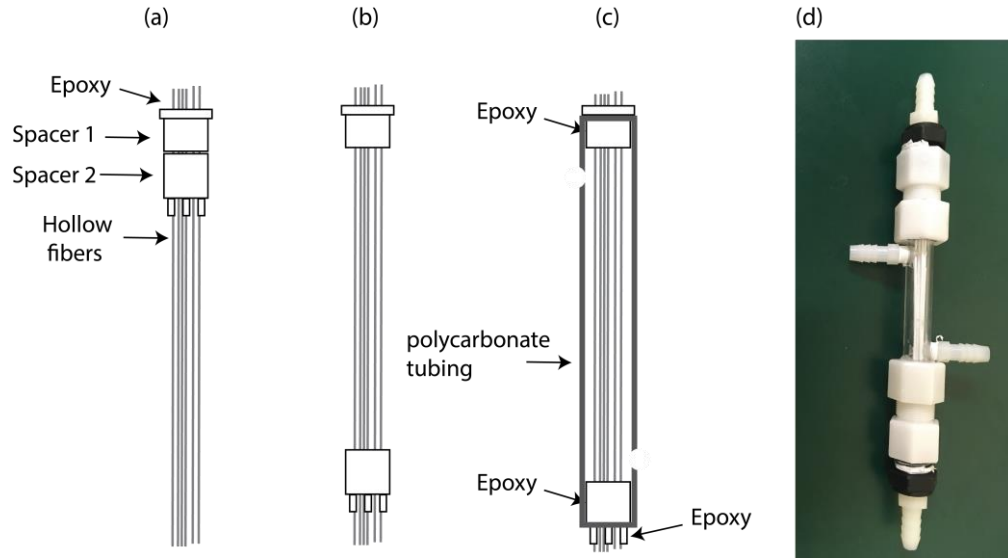
Figure 3.3 Illustration of module packing procedure.

The packing density of the module can be calculated using Eq. (3.5)

$$\varphi = N_{fibers} \frac{\left(O.D._{fiber}\right)^2}{\left(I.D._{tube}\right)^2}$$

(3.5)

φ is the packing density, N_{fibers} is the number of fibers, and *I.D.* and *O.D.* are the inner and outer diameters, respectively.

3.8 Membrane Distillation Performance

The flat sheet and hollow fiber membrane modules were tested in a DCMD setup, the schematic is shown in Figure 3.4. The streams were circulated using variable speed gear pumps. A synthetic feed with a concentration of 0.6 M NaCl (35 g/kg) was preheated, and the distillate (DI water) was precooled using hot and cold baths, respectively. The flow rates were measured using float style flow meters. The water flux, J , was measured by recording the accumulation of mass in the distillate tank. The concentration of salt in the distillate was monitored by measuring the ionic conductivity using a conductivity meter

(CON 2700, Oakton Instruments, IL, USA). The salt rejection was determined using Eq. (3.6) [21]

$$R_{NaCl} = \left(1 - \frac{V_D C_D}{C_F J A_m t}\right) \times 100 \tag{3.6}$$

where V_D is the volume of the distillate stream, C_D and C_F are the concentrations of salt in the distillate and the feed, respectively, A_m is the area of the membrane, and t is time.
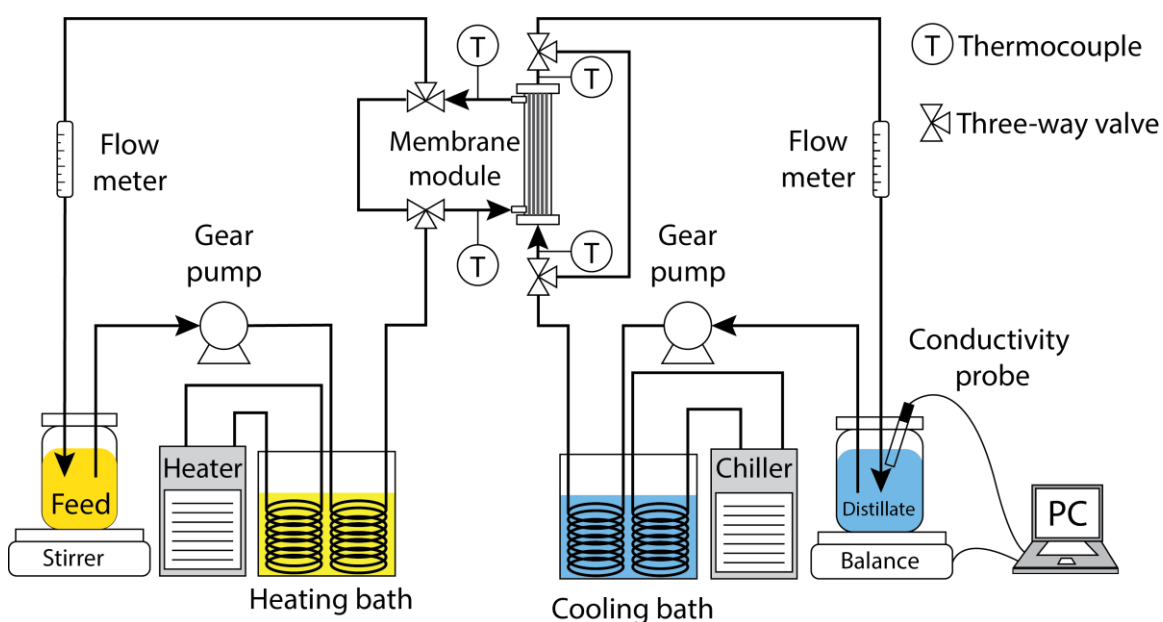
Figure 3.4 Schematic of a laboratory-scale DCMD setup.

The hollow fiber membranes were tested with surfactants and oil in the feed solution. The effect of surfactants was studied by sequentially adding sodium dodecyl sulfate (SDS) to a 0.3 M NaCl feed with an increment of 0.1 mM every hour until the concentration reached 0.4 mM. The effect of oil contamination was studied by preparing synthetic oil emulsion. Canola oil was vigorously stirred in 0.3 M NaCl and 0.07 mM SDS solution for 1 h to prepare solutions with concentrations of 100 and 500 ppm. The SDS

was added to stabilize the oil droplets and create the emulsion. The oil droplets were analyzed using an optical microscope (Axio Lab.A1, Zeiss, USA). The droplet size distribution was determined by performing an image analysis of the micrographs.

Chapter 4.   Results and Discussion

4.1   Flat Sheet Membranes

4.1.1   Membrane Characteristics

The flat sheet membranes we fabricated were macroporous (pore diameter > 50 nm) and macrovoid-free with sponge-like structures. Figure 4.1a shows the cross-section of a membrane fabricated with 70 v/v % IPA in the coagulation bath. The membranes that we fabricated with 30 and 50 v/v % IPA had similar bulk structures, as presented in Figure A.3a and b, respectively. Accordingly, the porosity of the membranes was relatively the same for all three membranes, as shown in Figure 4.2. The porosity of the 30, 50, and 70 v/v % membranes were 73.5% ± 0.1%, 76.1% ± 0.1%, and 77.5% ± 0.1%, respectively. This is owed to the delayed demixing in the phase inversion process. Delayed demixing yields desired porous structures for membrane distillation (MD), on the contrary, instantaneous demixing results in the formation of a dense skin layer and macrovoids that have been shown to hinder the flux in MD [32,80] and reduce the mechanical stability. It is important to note that the comparison between the rate of demixing is comparative and there is no clear definition of delayed and instantaneous demixing [81].

Water is considered a stronger nonsolvent for polyvinylidene fluoride (PVDF) than IPA because water has a weaker affinity to PVDF than IPA. This can be demonstrated by comparing the relative energy difference (RED) between water and PVDF (7.9) and IPA and PVDF (2.2) in Table 2.1. Therefore, the phase separation occurs relatively faster in a water-dominated medium when compared with that of an IPA-dominated medium.
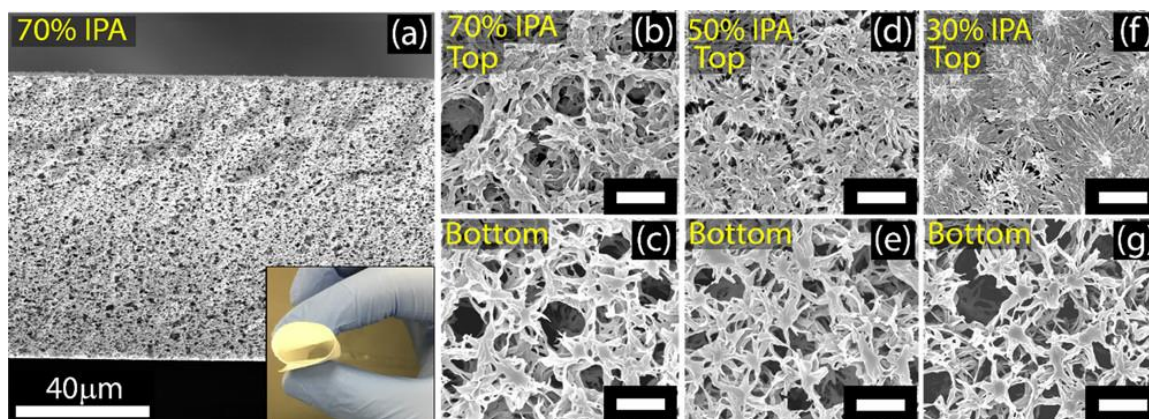
Figure 4.1 SEM images of pristine flat sheet membranes fabricated using different IPA compositions for the nonsolvent. (a) Cross-section image and (b) top and (c) bottom (glass side) surfaces of the membrane fabricated in a nonsolvent bath composed of 70 v/v % IPA in water; the inset shows that the membrane is sturdy and rollable. (d,e) SEM images of the (d) top and (e) bottom surfaces of a membrane made in 50 v/v % IPA in DI water. (f,g) SEM images of the (f) top and (g) bottom surfaces of a membrane made in 70 v/v %, IPA in DI water. The composition of the polymer solution was 12 wt. % PVDF (530 kDa) in TEP. The scale bars for (b–g) are 2 μm [53].

A dense skin layer (however, still porous) was present on the top surface of the membrane when the coagulation bath was 30 v/v % IPA, as presented in Figure 4.1f. When the concentration of IPA in the coagulation bath increased, the dense layer was eliminated and the top surface of the membranes appeared to be more porous, as shown in Figure 4.1b and d for 70 and 50 v/v % membranes, respectively. Although using 30 v/v % IPA as a coagulant yielded a denser outer surface, the bulk has similar porosity to the membranes produced with 50 and 70 v/v % coagulation baths. This is because the demixing is delayed as the coagulation bath diffuses into the cast film [81]. Consequentially, the bottom surfaces of the membranes have similar morphology, as shown in Figure 4.1c, e, and g.
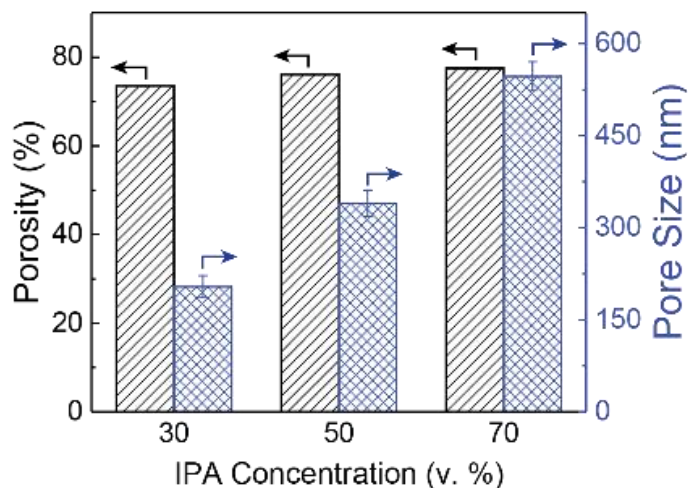
Figure 4.2 The effect of coagulation bath composition on the porosity and pore size distribution of flat sheet membranes [53].

To analyze the pore size of the flat sheet membranes, we performed the dry/wet flow method, also referred to as the gas/liquid promotery or the capillary flow porometry [30,90]. We performed the measurement using the "pressure step/stability" method, which offers higher precision and accuracy compared to the "pressure scan" method [90]. The wet and dry curves of all three flat sheet membranes are presented in Figure A.4 in Appendix A. Using the calculations that are reported in literature [30,92], we can find the pore size distribution from the dry and wet curves. The mean pore size of the membranes increased according to the increase in the pore size of the top surface, as shown in Figure 4.2 and the SEM images (Figure 4.1). The pore size of 30, 50, and 70 v/v % IPA coagulation baths were 203 nm ± 18 nm, 340 nm ± 21 nm, and 527 nm ± 24 nm, respectively. This technique measures the smallest diameter of the pore, which is referred to as the pore throat [90]. It is clear from the SEM analysis that the smallest pore diameter is located on the top surface; therefore, the measured pore size can be assumed to represent the size of the pores on the top surface.
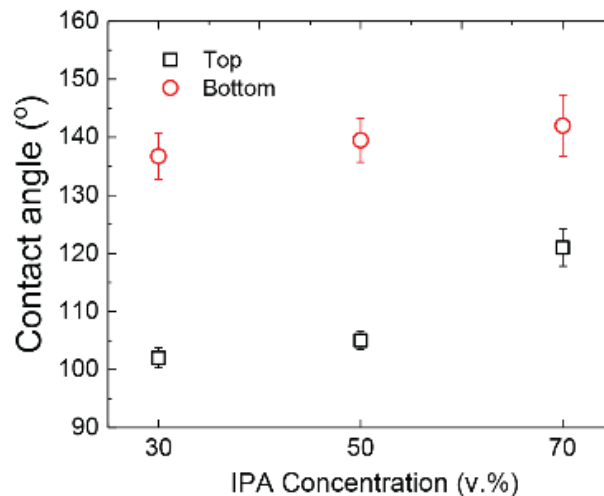
Figure 4.3 The effect of coagulation bath composition on the contact angle of the top and the bottom surface of the flat sheet membranes [53].

Figure 4.3 shows the contact angle on the top and bottom surface of membranes cast using different concentrations of IPA in the coagulation bath. As the IPA concentration in the coagulation bath was increased from 30 to 70 v/v %, the contact angles on the top surface were increased from $102 \pm 1.72°$ to $121 \pm 3.2°$, respectively. However, minimal changes in the contact angles for the bottom surfaces of the membranes were observed. We attributed this phenomenon to the topography of the surfaces of the membranes, as shown earlier in Figure 4.1. The induced rough texture traps air pockets at the air–water–membrane interface, creating a stable Cassie–Baxter nonwetting state [93].

4.1.2 Membrane Performance

We tested the flat sheet membranes in direct contact membrane distillation (DCMD) operation in feed temperature of 70 °C and distillate temperature of 20 °C to yield a differential vapor pressure difference ~40 kPa. The flow rates of the feed and distillate were set to 0.8 L min^{-1}. The gas permeation of the flat sheet membranes was performed under a set differential pressure of ~40 kPa. The nitrogen flux increased by ~50% and the

water flux in DCMD increased by ~40% when the concentration IPA in the coagulation bath increased from 30 to 70 v/v %. We attribute this to the increase in surface porosity and pore size distribution for the membranes fabrication with higher IPA concentration in the coagulation bath [39,80]. The pore size is directly related to permeation of gases inside a porous partition [30,94,95].
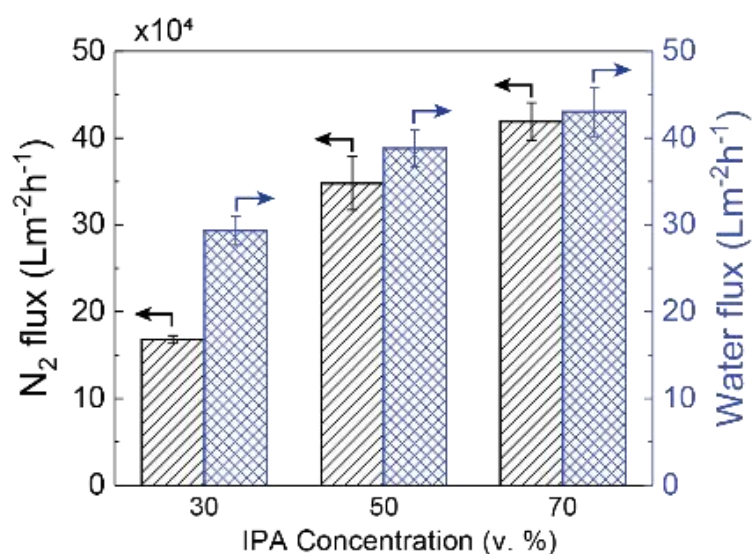
Figure 4.4 The effect of coagulation bath composition on the flux of nitrogen gas and water vapor in DCMD. The differential pressure and differential vapor pressure across the membrane was ~40 kPa [53].

4.2 Hollow Fiber Membranes

4.2.1 Membrane Properties and Characteristics

Figure 4.5a shows the cross-section of the fiber. The inner and outer diameters of the hollow fiber membrane are 1.1 and 0.82 mm, respectively. The fabricated hollow fiber membranes were macroporous and free of macrovoids with sponge-link structures and porosity of 72.2%. The formation of such structures is owed to the delayed phase separation. Macrovoid formation is caused by fast precipitation of the polymer in the

coagulation bath [78,81]. The precipitation rate can be delayed by adding a solvent into the coagulation. The presence of solvent lowers the activity of the nonsolvent (water) and limits the diffusion rate into the extruded polymer dope.

The outer and inner skins of the fiber appear to be slightly denser than the bulk of the fiber, as shown in Figure 4.5b and d, but still porous as shown in Figure 4.5c. This is due to the relatively faster precipitation rate near the polymer solution and coagulation bath interface compared to the bulk of the hollow fiber. As the nonsolvent diffuses into the polymer solution, the precipitation rate slows down and a relatively more porous bulk is obtained [81]. We observed a similar phenomenon with the flat sheet membranes (Section 4.1.1). The mean pore size of the outer surface of the pristine hollow fiber was measured to be ~110 nm (see Figure A.5, Appendix A).

We enhanced the surface properties of the hollow fibers by coating them with polytetrafluoroethylene (PTFE) and poly (1H,1H,2H,2H-perfluorodecyl acrylate) (pPFDA) in an initiated chemical vapor deposition (iCVD) reactor using a novel procedure (patent pending). Other researchers also used iCVD to coat low surface energy materials on hydrophilic membranes to make them applicable for MD [91,96,97]. We coated the fibers with PTFE in the iCVD reactor to produce rough texture, then coated them with pPFDA to reduce the surface energy. (The hollow fibers that were coated in iCVD reactor are referred to here as "coated"). Using image analysis on the inset of Figure 4.5d, the thickness of the coating was measured to be ~1 μm.
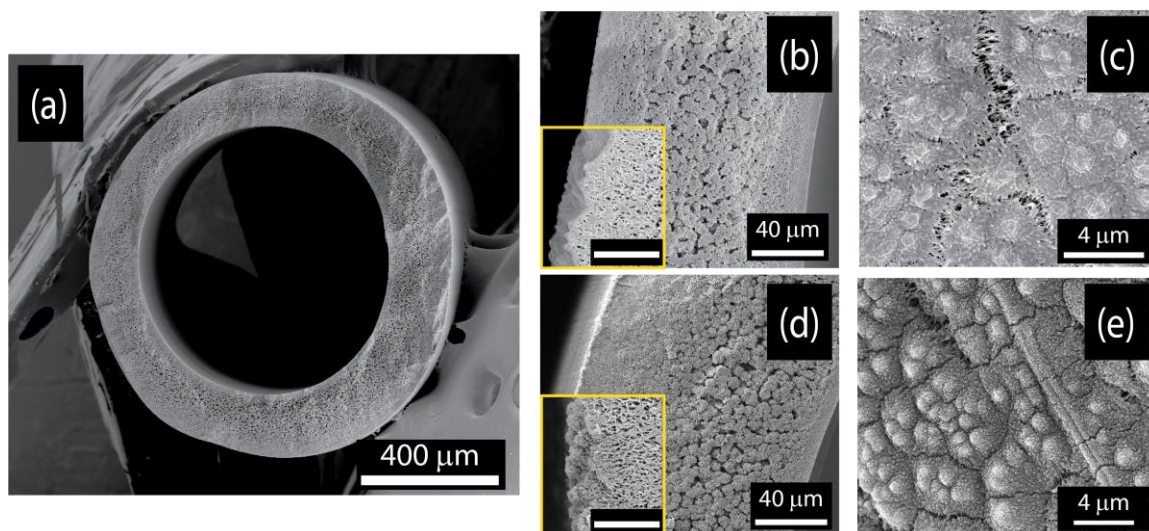
Figure 4.5 SEM images of (a-c) pristine and (d-e) coated hollow fiber membranes. (a) Cross-section image of the hollow fiber membrane. The wall of the (b) pristine and (d) coated membrane. The image of the outer surface area of the (c) pristine and (e) the coated membrane. The insets in (b) and (d) show the high magnification micrographs of the outer surface, with a scale bar equal to 5 μm.

Figure A.7 displays the wettability of the coated and pristine membrane in water, ethylene glycol, canola oil, and ethanol. The pristine hollow fiber membrane was wetted with ethylene glycol, canola oil, and ethanol with an apparent contact ~26°, ~20°, and ~10°, respectively. On the other hand, the coated hollow fibers showed better wetting resistance than the pristine membrane. The downward curvature of water was larger for the coated hollow fiber than the pristine one for water. The size of curvature decreased as the surface energy of liquid decreased, until it was completely wetted in ethanol with an apparent contact angle of ~10°.

Figure A.6 shows the FTIR spectra of the coated and pristine membranes. The spectrum of the pristine membrane shows the peak of CH_2 bending at 1400 cm^{-1}. The intensity of the same peak declined for the coated membrane because the surface was

coated with PTFE and pPFDA. Also, the peak at 1170 cm^{-1} is associated with the CF$_2$ stretching band in PVDF. The coated fiber had two peaks in that wavenumber region associated with asymmetrical and symmetrical stretching of the CF$_2$ band. The peak at ~1800 cm^{-1} in the coated membrane spectra is associated with C=O stretching band of pPFDA.

4.2.2 Gas Permeation

We characterized the gas permeation of the hollow fiber membrane using nitrogen gas. We performed the permeation test to compare the flux of nitrogen gas through the pristine and coated membrane. The value of B$_g$ of each membrane can be obtained by fitting the permeation data to Eq. (3.4) using linear regression analysis and assuming a linear relationship between the pressure and flux in the working pressure range. The value of B$_g$ for pristine and coated hollow fiber are presented in Figure 4. B$_g$ declined by ~40% after coating the hollow fibers due to the blocking of the pores on the outer surface. The coating decreased the surface porosity of the hollow fibers, which reduced the gas flux [39,80]. Since MD is governed by the diffusion of water vapor through the pores of the membrane, the comparison between the nitrogen gas fluxes is a good predictor of the MD performance of the membrane. A typical DCMD operates in a differential vapor pressure range of 20-40 kPa.
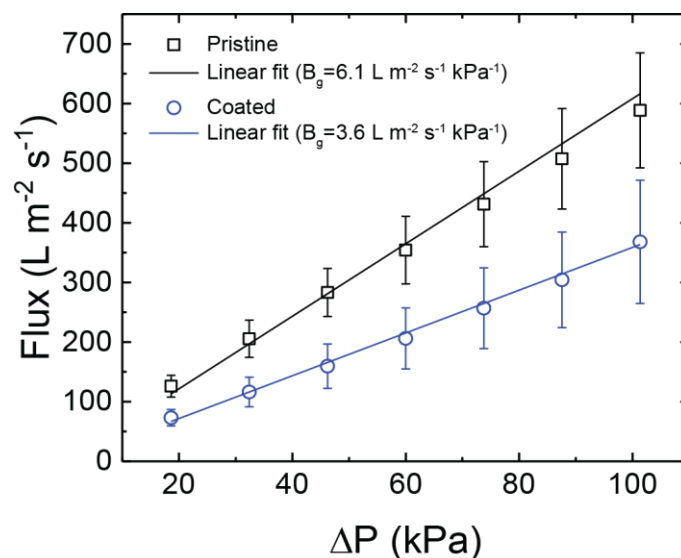
Figure 4.6 Gas permeation of the pristine and coated hollow fiber membrane. The correlation factors, R^2, for the pristine and coated hollow fiber membrane were 0.9966 and 0.9972, respectively.

4.2.3 Membrane Packing

We packed the hollow fiber membranes so that the outer surfaces were not in contact with each other. Our design was adopted from Mohammadi Ghaleni et al. [98] who showed, using multiphysics simulation, that the DCMD flux declines when the fibers are in contact with each other due to the overlap of thermal boundary layers across the membrane. Using the procedure discussed in Section 3.7, we can pack the hollow fibers with controllable distance from each other by designing 3D modeled spacers (Figure A.1 and Figure A.2) using CAD software (SpaceClaim). We have easy control over the distance between fibers by manipulating the design of the spacers using additive manufacturing. The modules prepared for this work were 10 cm long and contained 13 or 7 hollow fibers. Our initial design (Module 2 in Figure 4.7a) offered poor water production rate per volume of packing due to the dead volume. We modified the design by using a smaller tube and packed the same number of fibers. We observed an 80% increase in the water production

rate per volume of packing, even though the flux was the same, as presented in Figure 4.7b and c. Therefore, we used Module 1 for the remaining experiments.
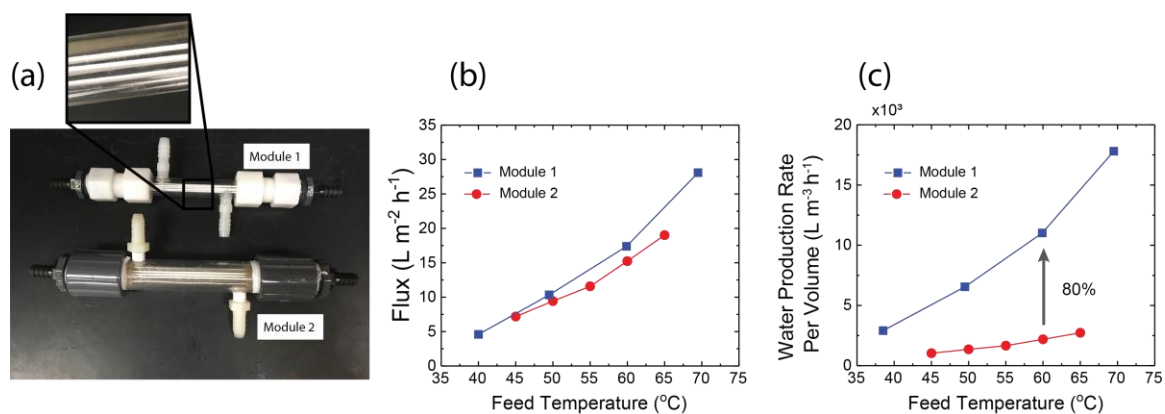
Figure 4.7 Effect of module packing on the water production rate per volume of packing for modules prepared using the same number of fibers (13). (a) An illustration of modified design (Module 1) and initial design (Module 2). The inset shows the distance between the fibers inside the module. (b) The effect of feed temperature on the flux. (c) The effect of feed temperature on the water production rate per volume of packing.

The number of fibers packed in the modules defines the packing density of the module, according to Eq. (3.5). With high packing density, there is a higher surface area of hollow fiber membrane for heat transfer in the module. Higher heat transfer leads to a reduction in driving force along the axial position of the module. This can be demonstrated by analyzing the flux of pristine membrane modules with 17.3% and 9.3% packing density, shown in Figure 4.8.
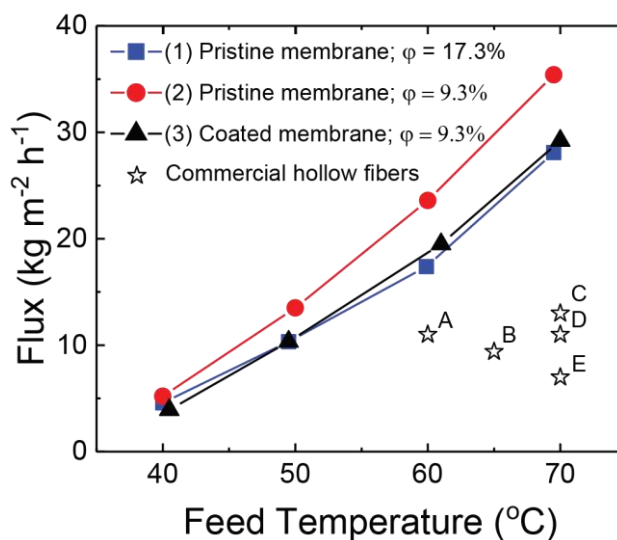
Figure 4.8 The effect of feed temperature on the flux of three modules: (1) Module packed with pristine membranes with packing density of 17.3%, (2) module packed with pristine membranes with packing density of 9.3%, and (3) module packed with coated membranes with packing density of 9.3%. The feed and distillate flow rates for all experiments were set to 0.4 L min^{-1}. The temperature of the distillate was set to 19 °C. (A: Chew et al. [38], B: Huang and Arning [73], C: Al-Obaidani et al. [99], D: Driolo et al. [74], and E: Teoh et al. [100]).

As shown in Figure 4.8, the flux of the module packed with coated hollow fibers is lower compared to the module packed with pristine hollow fibers. We can attribute the lower water vapor flux to the reduction in surface porosity of the hollow fiber membranes after coating. Furthermore, the fluxes of hollow fiber membrane modules of this work are higher than the reported fluxes of commercial hollow fiber packages [38,73,74,99,100], as displayed in Figure 4.8. The characteristics of the commercial hollow fiber membranes and their vendors are presented in Table 4.1. We can see that the commercial membranes suffer from low porosity and large membrane thickness compared to the hollow fiber membrane fabricated in this study.

Table 4.1 Commercial hollow fiber membranes from Figure 4.8.

ID	Material	Porosity	Mean pore size	Thickness	Vendor	Reference
A	PVDF	83%	22 nm	330 μm	N.A.	[38]
B	PTFE	50%	495 nm	178 μm	Markel Corp., PA, USA	[73]
C	PP	70%	200 nm	650 μm	Microdyn-Nadir, Germany	[99]
D	PP	70%	200 nm	450 μm	Membrana, Germany[a]	[74]
E	PP	35%	150 nm	55 μm	Hyflux, Singapore	[100]
	PVDF	72%	110 nm	140 μm		This work

a: currently 3M Separation and Purification Division

4.2.4 Effect of Surfactant

Surfactants, such as sodium dodecyl sulfate (SDS), are amphiphilic organic compounds consisting of a hydrophobic tail and a hydrophilic head. When they are present in an aqueous solution, they diffuse towards the liquid/air interface, which results in a decrease in solution surface tension. Wetting in membrane distillation membranes is governed by the liquids entry pressure (LEP), which is described by the Young-Laplace equation (Eq. (3.3)). Since the presence of SDS lowers the surface tension at the liquid-gas interface, the LEP of the solution decreases and wetting occurs.

To investigate the desalination performance of the pristine and coated membranes in a feed solution with lower surface energy than water, we added 0.1, 0.2, 0.3, and 0.4 mM SDS to the 0.3 M NaCl feed to lower the surface tension to ~54, ~47, ~43, ~39 mN m^{-1} [101]. Neither the pristine nor the coated hollow fibers showed any sign of wetting throughout the 9 h of DCMD operation, as displayed in Figure 4.9. Both membranes

maintained a normalized flux close to unity and a ~100% salt rejection. We performed a similar test on the flat sheet membrane that was fabricated with 70 v/v % IPA in the coagulation bath. The membrane started wetting in 0.2 mM SDS as the flux started declining and the salt rejection started to decrease. The distillate flux and salt rejection further declined after adding 0.3 and 0.4 mM until the flux decreased to 80% of the initial flux and the salt rejection decreased 96% after an hour of adding 0.4 mM SDS, as displayed in Figure A.9, indicating partial wetting. In partial wetting, the decline in flux is attributed to the reduction of the differential interfacial temperature (temperature polarization [41]) due to the penetration of water into the membrane. The decline in salt rejection is due to the crossing of the saline feed into the distillate side due to the wetting of some of the pores of the membrane (see Section 2.2).

Figure 4.9 Normalized water flux and salt rejection of the pristine membrane ($\varphi = 9.3\%$) and the coated membrane ($\varphi = 9.3\%$) with varying concentration of SDS in the feed. 0.1 mM SDS was sequentially added to the feed every hour until the concentration reached 0.4 mM. The feed and distillate temperatures were set to 50 and 19 °C, respectively. The flow rate of feed and distillate were set to 0.4 L min^{-1}. J_0 of the pristine and coated membranes were 14.3 and 9.25 L m^{-2} h^{-1}, respectively.

The wetting resistance of the hollow fiber membranes can be attributed to two factors: Firstly, the small pore size of the outer surface of the fibers leads to higher LEP. Even though the surface tension at the liquid-gas interface decreased due to the presence of SDS, it is not sufficient to penetrate the small outer surface pores of the hollow fibers (110 nm). On the other hand, the flat sheet membrane that was fabricated using 70 v/v % IPA in the coagulation bath has significantly larger pore size on the outer surface (527 nm), which led to wetting of some pores. Secondly, the hydrophobic tail of the surfactant adsorbs to the surface of the membrane surface due to nonpolar interactions between the molecules of the two molecules (polymer and surfactant). This lowers the number of surfactant molecules near the liquid-gas interface at the membrane pore, which

consequentially leads to higher surface tension at the vicinity of the pore and increases the LEP [102].

4.2.5 Effect of Oil Emulsion

Oilfield-produced water typically contains 2-565 mg L^{-1} [21,38,103], with oil droplet size in the range from 2 to 30 μm [38]. MD is a potential candidate for the treatment of oilfield-produced water because it offers ~100% rejection of nonvolatile components [21,43,48,49,53]. To evaluate the durability of our fabricated modules, we prepared a synthetic oil emulsion that simulates oilfield-produced water, as described in Section 3.8. Figure 4.10a shows that the emulsions were foggy compared to pure water. We didn't observe any phase separation for the emulsion after 48 h of relaxing the solution, which indicated the stability of the emulsions. Using image analysis on the micrographs of the emulsions (Figure 4.10b and c), we obtained the histogram of the droplet size distribution. The histograms show that the distribution of droplet size is wider in higher oil concentration; however, the mean droplet size was relatively similar (~5 μm). The largest droplet size was ~23 μm for 500 ppm, compared to ~12 μm for 100 ppm.
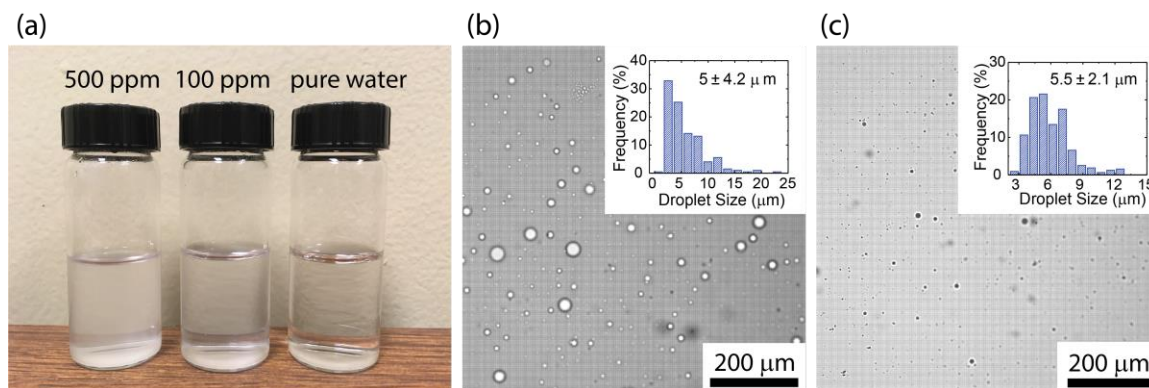
Figure 4.10 (a) Samples of 500 ppm, 100 ppm oil, and pure water. Optical microscopic image of (b) 500 ppm oil emulsion and (c) 100 ppm oil emulsion. The insets in (b) and (c) display the size of oil droplets using image analysis on the micrographs.

Neither the pristine nor the coated hollow fibers fouled when they were challenged with 100 ppm oil, as displayed in Figure 4.11a. The normalized flux was close to unity for both membranes and the salt rejection was ~100%. We attribute this to the electrostatic repulsion between the hydrophilic head of SDS and the membrane material as well as the low amount of oil droplets in the solution. On the other hand, the normalized flux of the modules declined with similar time constants when in 500 ppm oil-contaminated feed, as displayed in Figure 4.11b. The normalized flux steadied at a value of 0.3 after 12 h of experiment, which meant oil started blocking the membrane pores, inhibiting water vapor to enter the pores. The salt rejection of the pristine hollow fiber declined to 98% after 16 h of DCMD operation; however, the rejection of the coated hollow fiber remained at 99.8%. This indicates superhydrophobicity of the coating that did not allow for water to wet the pores even after they were fouled with oil; on the other hand, the fouling caused the pristine membrane to wet and feed flowed through the membrane pores.
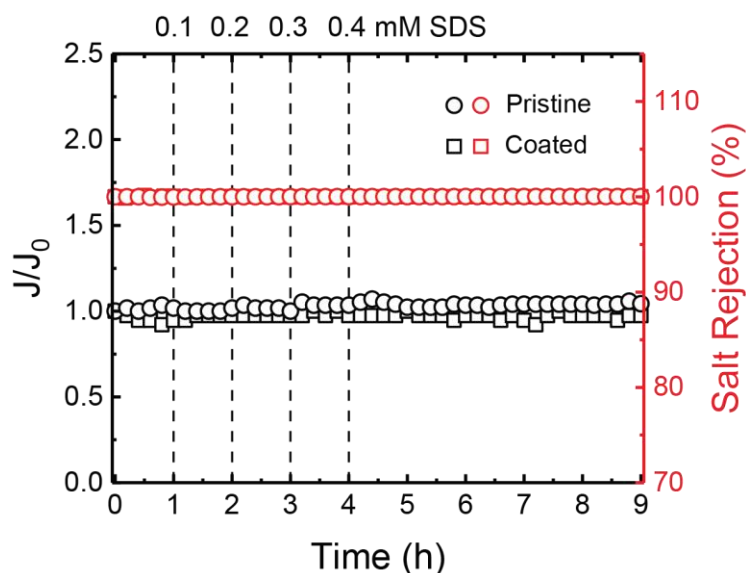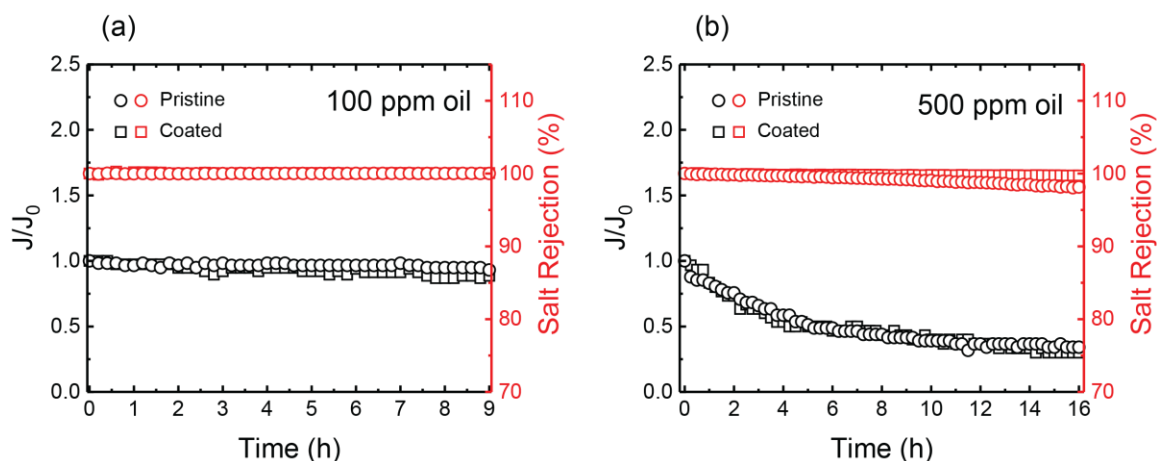
Figure 4.11 Normalized water flux and salt rejection of the pristine membrane (φ =9.3%) and the coated membrane (φ =9.3%) in (a) 100 ppm and (b) 500 ppm oil-contaminated feed solution. The feed and distillate temperatures were set to 50 and 19 °C, respectively. The flow rate of feed and distillate were set to 0.4 L min^{-1}. J$_0$ of the pristine and coated membranes were 14.5 and 9.5 L m^{-2} h^{-1}, respectively, for (a), and 10.25 and 8.15 L m^{-2} h^{-1}, respectively, for (b).

The fouling occurs due to nonpolar interaction between oil molecules and the membrane surface. Designing a surface that repels oils requires not only a low surface energy material but also a rough texture. The effect of roughness on the wetting of porous surfaces has been studied by Wenzel [104] and Cassie and Baxter [105]. Wenzel's model recognizes that the surface roughness increases the available surface area of the solid, and the liquid penetrates through the rough structures. On the other hand, Cassie's model postulates that the liquid is repelled due to the microscopic pockets of air trapped inside the rough texture. Scientists later discovered that the liquid can irreversibly transition from the Cassie to the Wenzel state [93]. For the oil to be repelled by the reentrant structures, it needs to remain in a Cassie-Baxter state. The reentrant structures created on the hollow fiber membrane using an iCVD reactor in addition to the low surface energy pPFDA were

not sufficient to repel the oil in DCMD operation (Figure 4.11b), even though the static test showed that the oil did not wet the coated hollow fiber (Figure A.7).
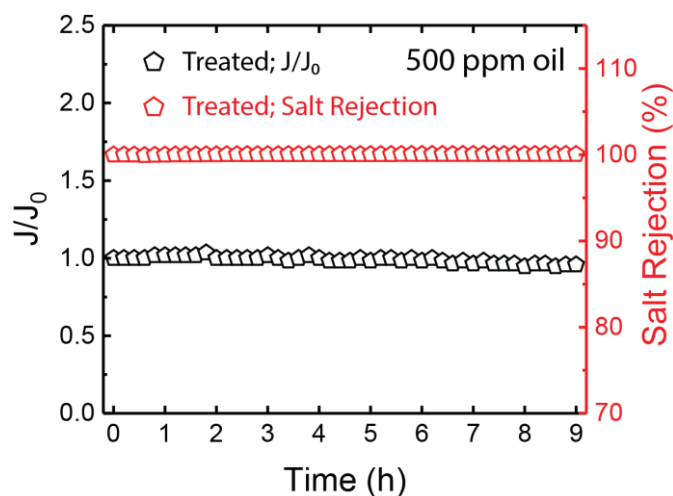
Figure 4.12 Normalized water flux and salt rejection of the treated hollow fiber membrane module (φ =9.3%) in 500 ppm oil-contaminated feed solution. The feed and distillate temperatures were set to 50 and 19 °C, respectively. The flow rate of feed and distillate were set to 0.4 L min^{-1}. J_0 was 14.0 L m^{-2} h^{-1}.

To develop an anti-oil-fouling membrane, we terminated the outer surface of the PVDF with –OH groups using a method that we developed for flat sheet membranes [53] and modified for the hollow fiber membranes (see Section 3.5.2). The –OH groups on the outer surface have a strong interaction with water and weak interaction with oil. Consequentially, this yields a hydration layer on the surface of the membrane that repels oil droplets, creating an underwater-oleophobic membrane [43,44,46,47,53,106]. The treated hollow fibers displayed excellent anti-oil-fouling performance compared to the pristine and coated hollow fibers. Figure 4.12 shows the durable DCMD operation of a module with treated hollow fibers for 9 h. The appeal of our facile chemical treatment method is that it does lead to the decline in the flux of the modified membrane. The reported

modifications in the literature caused the decline in MD flux compared with the pristine membranes due to the blocking of the pores of the membrane by nanoparticles [44,46,47,107].

4.2.6 Salt Scaling

We studied the effect of coating on the salt scaling propensity of the outer surface of the hollow fiber membranes. We conducted an accelerated salt scaling experiment using a solution containing 20 mM of calcium and sulfate ions for 24 h to 60 ˚C. Figure A.10 shows the schematic of the accelerated salt scaling setup. Calcium sulfate crystallizes to form gypsum ($CaSO_4 \cdot 2H_2O$), which poses a significant challenge to thermal desalination processes due to the inverse relationship between its solubility and temperature [42]. The SEM images of the pristine and functionalized membrane after the scaling experiment are displayed in Figure 4.13a and b, respectively. The results show a clear difference in size and area coverage of the crystals deposited on the pristine and coated membrane. The area fraction of salt crystals on the pristine surface was 19.7% of the membrane surface area, as shown in Figure 4.13a, while it was less than 3% for the functionalized membrane surface, as shown in Figure 4.13b.
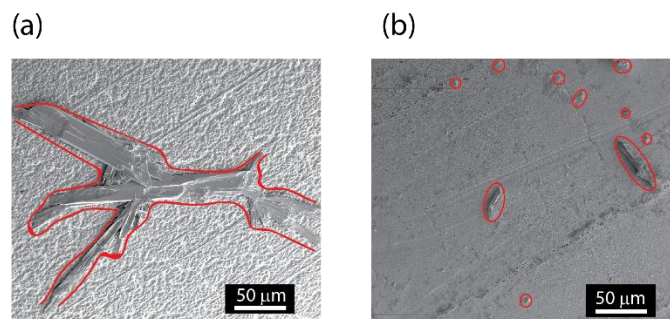
Figure 4.13 SEM images of outer surfaces of (a) pristine and (b) coated hollow fiber membrane after accelerated salt scaling experiment. The salt crystals on membranes are circled with a red line.

4.3   Conclusion

In conclusion, we showed that the structure of PVDF membranes can be adjusted by controlling the parameters of NIPS. By searching the space of parameters, membranes with desired MD performances can be fabricated. We have found that lowering the activity of the nonsolvent (by adding a TEP and IPA into the coagulation bath) delays the NIPS, allowing for the creation of membranes with high surface porosities and free of macrovoids. The formation of a dense layer at the interface of the polymer solution and the nonsolvent was hindered by lowering the activity of the nonsolvent (delaying the demixing process) in the coagulation bath by controlling the composition. By eliminating the skin layer, we produced membranes with larger surface porosity and pore size that are suitable for MD.

Because hollow fiber membrane packages offer higher membrane packing density, when compared with plate and frames and spiral wounds, we fabricated hollow fiber membranes using our developed formulations and evaluated the wetting and fouling propensity of the hollow fiber membranes as well as their performance in DCMD.

Additionally, we imparted superhydrophobic and underwater-oleophobic properties to the hollow fiber membranes by applying a thin coat of highly hydrophobic materials (PTFE and pPFDA) and terminating the fluorine in PVDF with –OH groups to the outer surface of the membranes, respectively. The pristine and coated hollow fibers showed excellent anti-wetting performance when challenged with surfactants. Also, they did not show any sign of fouling in a low concentration of oil (100 ppm). However, they both fouled when they were challenged with a high amount of oil (500 ppm). This suggests that the superhydrophobic membranes in a mixture of water and oil would not be a proper choice for membrane materials. On the contrary, the underwater-oleophobic showed superior anti-oil-fouling performance, which indicates that membranes with hydrophilic outer surfaces are the best choice for the treatment of oil-contaminated water streams using MD.

Chapter 5.   Recommendation for Future Work

5.1   Membrane Fabrication

The performance and durability of the hollow fiber membranes ought to be further explored. It is clear from the experimental results that robust membrane distillation (MD) operation requires membranes with porous bulk and small pore size of the outer surface. The increase in surface porosity was shown to enhance the flux of the membrane; however, with the increase in surface porosity, the pore size of the outer surface increased. Fabricating a membrane with high surface porosity while maintaining a narrow outer surface pore size is expected to yield good and durable MD performance. Moreover, the effect of hollow fiber wall thickness would be an interesting parameter to explore. Bonyadi et al. observed enhancement in MD flux when the thickness of the hollow fiber membranes decreased from 100 to 50 μm [32]. However, they did not study the effect of thickness on the mechanical integrity of the fibers.

The space parameters of the nonsolvent induced phase separation (NIPS) should be investigated in a roll-to-roll process [88]. Many factors need to be considered to transition to a full-scale dry-jet wet spinning apparatus; for instance, using a large amount of solvent in the coagulation bath would not be favorable [32]. Therefore, it is important to explore NIPS for the mass fabrication of PVDF hollow fiber membranes for MD and accounting for the environmental, economic, and process limitations.

Several improvements to the characterization of the hollow fiber membranes can be made. The pore size distribution of the hollow fiber membranes naad be analyzed using the dry/wet method. A procedure ought to be developed to measure the dry and wet curves for the hollow fiber membranes. The dynamic contact angle provides a comprehensive

study on the wettability of the hollow fiber membranes compared to the static contact angle measurement. The dynamic contact angle can be measured using force tensiometers [57,75]. The treated hollow fiber membranes need to be further characterized.

5.2   Solar-Assisted Membrane Distillation

MD is an energy-demanding process. Mistry et al. compared the thermodynamic efficiency of a typical direct contact membrane distillation (DCMD) operation with other desalination technologies and found it to be lower [108]. However, the calculations were performed for fixed and assumed DCMD parameters. The efficiency can be improved significantly by optimizing the MD process. S. Lin et al. studied the effect of MD process parameters [109] and A. Deshmukh et al. membrane property parameters [110] on the energy performance of MD process using ordinary differential equation (ODE) modeling and reported thermodynamic optima of these parameters. The ODEs of the DCMD process using a hollow fiber membrane module are derived in Appendix C.
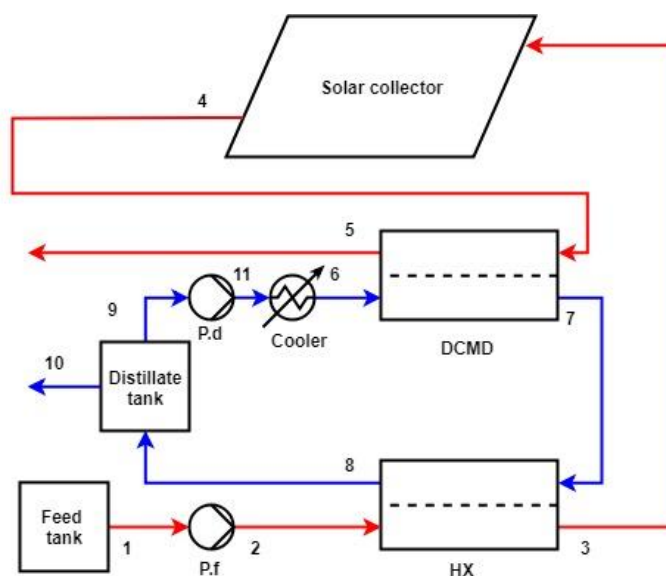
Figure 5.1 Schematic of solar-assisted MD

Figure 5.1 shows a typical hollow fiber MD process powered by solar energy with heat recovery. The process is adapted from previous studies [109,111] with the addition of a solar collector (SC) as a heat source. The first and second law of thermodynamics for the DCMD unit, SC, a heat exchanger (HX), and cooler are derived in Appendix B. For a typical MD operation, the specific entropy generation of the system was estimated to be 2871 J kg^{-1} K^{-1} for 1000 kg per day of water production. The SC was the major contributor to the total entropy generation (~90%), followed by the DCMD module (6%). Figure 5.2 shows that the entropy generation associated with the DCMD module can be reduced by increasing the length of the module. It is important to note that the flux decreased with the increase in module length due to the decrease in the driving force along the axial position of the module, however, the water production increased which led to a lower specific entropy generation.
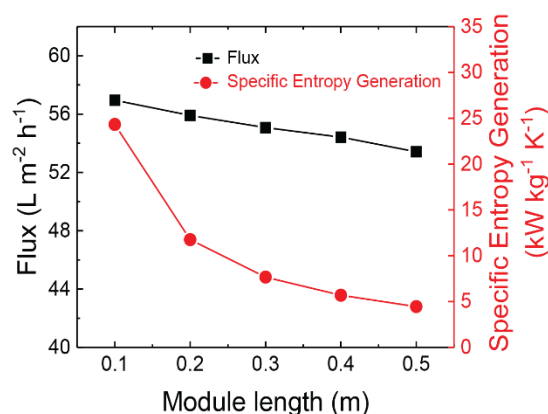
Figure 5.2 Effect of module length on the flux and specific entropy generation of the hollow fiber membrane. The calculations were performed on simulation data obtained from [98].

Solar thermal energy collectors have inherently low thermodynamic efficiency due to heat losses to the environment and large temperature difference between the heat source

(sun) and the working fluid. Indeed, a study of the thermodynamics would not be complete without associating the cost. Therefore, a comprehensive study is needed to relate the energy efficiency of the solar-assisted MD process with the predicted cost of the system. However, due to the uncertainty in energy and cost predictions of MD processes [28], relating the energy and cost estimations would not be valid until MD membranes and modules are commercialized.

Appendix A. Supporting Data

Side View   Top View   Side View   Top View
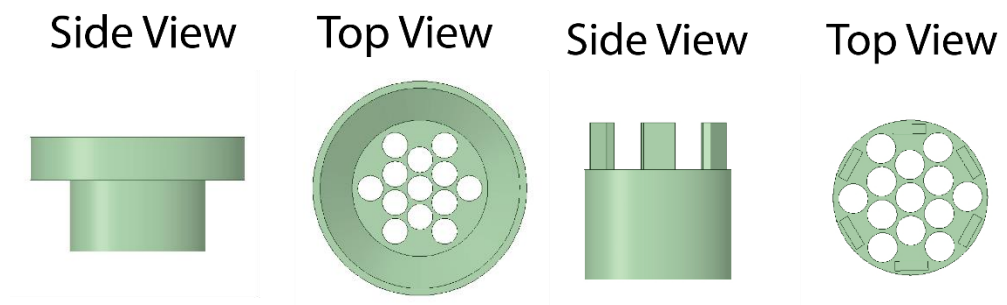
Figure A.1 Geometry of Spacer 1   Figure A.2 Geometry of Spacer 2.

(a)   (b)
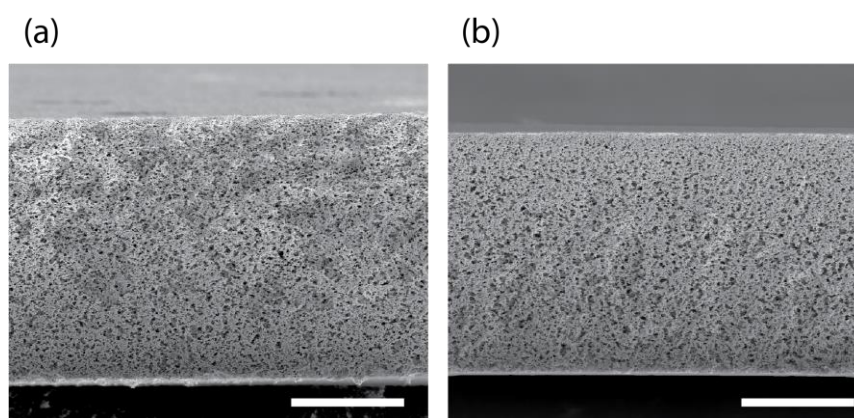
Figure A.3 Cross-section of PVDF membranes fabricated using (a) 30 v/v % IPA and (b)

50 v/v % IPA in the coagulation bath. Scale bar is 40 μm in both images.
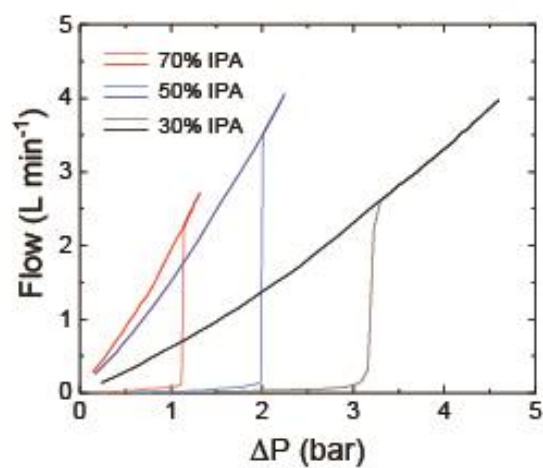
Figure A.4 Dry and wet curves for pore size distribution analysis of the flat sheet membranes.

(a) Pristine

(b) Coated

(c)
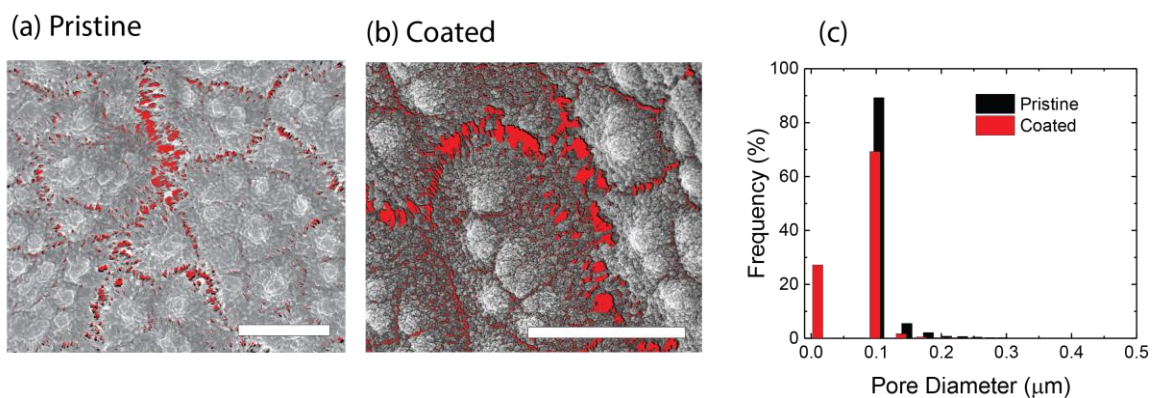
Figure A.5 Pore size distribution analysis on the pristine and coated hollow fiber membrane. SEM images of (a) pristine and (b) coated hollow fiber membrane. Scale bars in (a) and (b) are 4 and 5 μm. (c) pore size distribution using image analysis on (a) and (b). The mean pore sizes for the pristine and coated hollow fiber membrane were 0.11 and 0.077 μm, respectively.
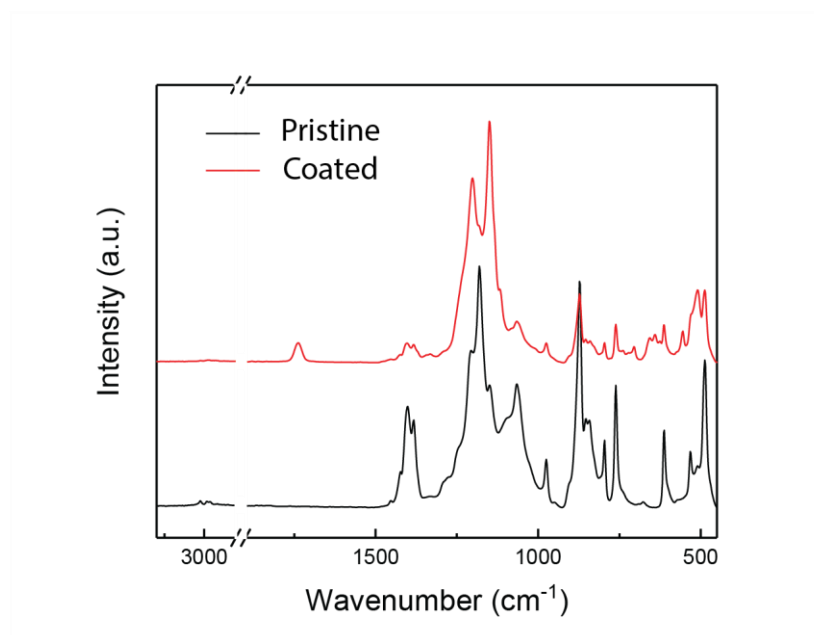
Figure A.6 FTIR of Pristine and coated hollow fiber membrane
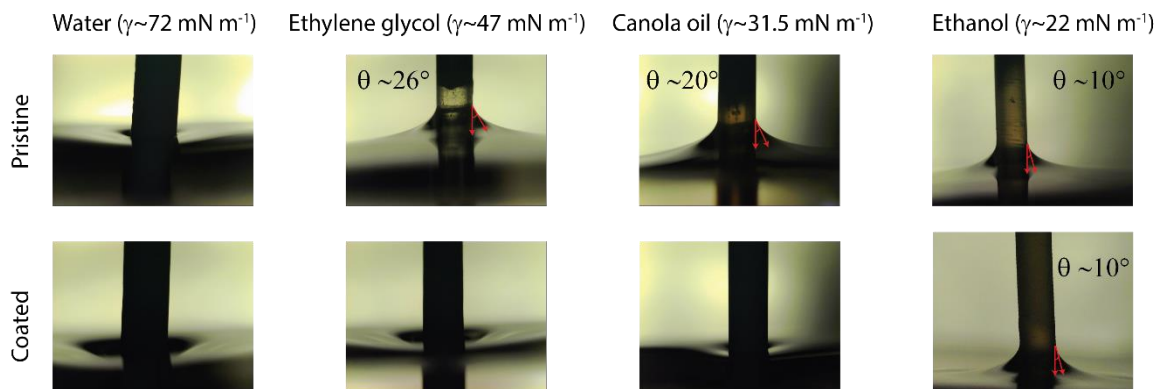
Figure A.7 Wettability of the pristine and coated membrane with different liquids.
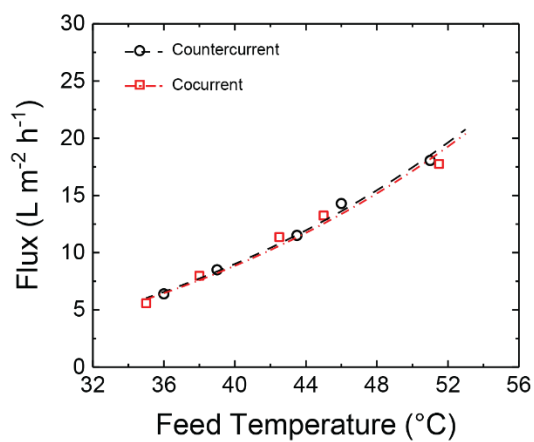
Figure A.8 Effect of countercurrent and concurrent configuration of the flux of the module
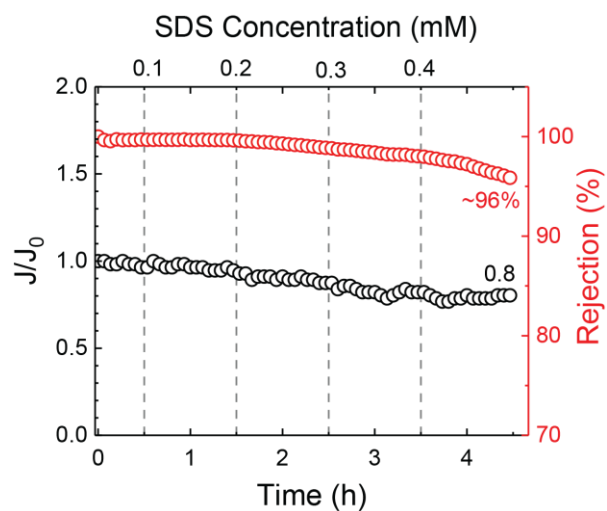
Figure A.9 Effect of SDS on the performance of a flat sheet membrane (70 v/v % IPA in the coagulation bath). For feed temperature of 70 °C, J_0 was 35 L m^{-2} h^{-1}.
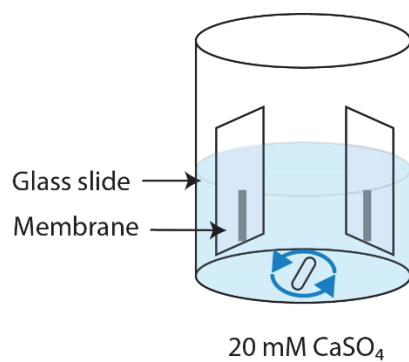
Figure A.10 Accelerated salt scaling experiment. The temperature of the solution was set to 60 °C.

Appendix B. Thermodynamics of Solar Assisted Membrane Distillation

Applying the first and second law of thermodynamics to the DCMD module (Eqs. (B1) and (B2)), heat exchanger (HX) (Eqs. (B3) and (B4)), solar collector (SC) [112] (Eqs. (B5) and (B6)) and cooler (Eqs. (B7) and (B8)) in Figure 5.1 (the subscripts correspond to the stream numbers in Figure 5.1). The following assumptions were made to derive Eqs. . (B1-B8) [112,113]:

- Pure and saline water are assumed to behave as incompressible fluids

- The HX, DCMD module, cooler, and SC were assumed to undergo isobaric temperature change

- The dependence of the specific heat capacity on temperature was neglected

- The HX, DCMD module, and cooler were assumed to be adiabatic

$$\dot{m}_4 c_p \left(T_4 - T_5 \right) + \dot{m}_6 c_p \left(T_6 - T_7 \right) + \dot{m}_{10} c_p \left(T_5 - T_7 \right) = 0 \tag{B1}$$

$$\dot{m}_4 c_p \ln\left(\frac{T_5}{T_4} \right) + \dot{m}_6 c_p \ln\left(\frac{T_7}{T_6} \right) + \dot{m}_{10} c_p \ln\left(\frac{T_6}{T_8} \right) = \dot{S}_{gen}^{DCMD} \tag{B2}$$

$$\dot{m}_7 c_p (T_8 - T_7) + \dot{m}_2 c_p (T_3 - T_2) = 0 \tag{B3}$$

$$\dot{m}_7 c_p \ln\left(\frac{T_8}{T_7} \right) + \dot{m}_2 c_p \ln\left(\frac{T_3}{T_2} \right) = \dot{S}_{gen}^{HX} \tag{B4}$$

$$\dot{m}_3 c_p \left(T_4 - T_3 \right) - \dot{Q}_S + \dot{Q}_0 = 0 \tag{B5}$$

$$\dot{m}_3 c_p \ln\left(\frac{T_4}{T_3} \right) - \frac{\dot{Q}_S}{T_S} + \frac{\dot{Q}_0}{T_0} = \dot{S}_{gen}^{SC} \tag{B6}$$

$$\dot{m}_{11} c_p (T_{11} - T_6) - \dot{Q}_{cooler} = 0 \qquad (B7)$$

$$\dot{m}_{11} c_p \ln\left(\frac{T_{11}}{T_6}\right) - \frac{\dot{Q}_{cooler}}{T_{cooler}} = \dot{S}_{gen}^{cooler} \qquad (B8)$$

Also considering temperature disequilibrium of streams 5 and 10 with the dead state temperature of the environment [108,113–115]

$$\dot{S}_{gen}^{disequilibrium} = \dot{m}_5 c_p \left[\ln\left(\frac{T_0}{T_5}\right) + \frac{T_5}{T_0} - 1\right] + \dot{m}_{10} c_p \left[\ln\left(\frac{T_0}{T_{10}}\right) + \frac{T_{10}}{T_0} - 1\right] \qquad (B9)$$

Total entropy generation

$$\dot{S}_{gen}^{total} = \dot{S}_{gen}^{DCMD} + \dot{S}_{gen}^{HX} + \dot{S}_{gen}^{SC} + \dot{S}_{gen}^{cooler} + \dot{S}_{gen}^{disequilibrium} \qquad (B10)$$

Specific entropy generation describes the reversibility of the process

$$\zeta_{gen}^{total} = \frac{\dot{S}_{gen}^{total}}{\dot{m}_{10}} \qquad (B11)$$

Appendix C. Modeling Membrane Distillation

(a) Counter-current   (b) Co-current
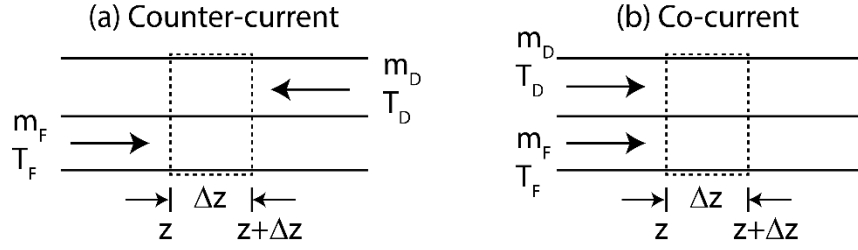
Figure C.1 Finite element analysis on DCMD process for counter- and cocurrent

The flux and differential area are described by Eqs. (C1) and (C2):

$$J = B_{MD} \left(P_F^{Sat} - P_D^{Sat} \right) \tag{C1}$$

$$\Delta A = N_{fiber} 2\pi R_o \Delta z \tag{C2}$$

For countercurrent configuration, energy balance on feed side (F) and distillate side (D) yields:

$$\dot{m}_F(z) - \dot{m}_F(z+\Delta z) - N_{fibers} 2\pi R_o \Delta z B_{MD} \left(P_F^{Sat} - P_D^{Sat} \right) = 0 \tag{C3}$$

$$\dot{m}_D(z+\Delta z) - \dot{m}_D(z) + N_{fibers} 2\pi R_o \Delta z B_{MD} \left(P_F^{Sat} - P_D^{Sat} \right) = 0 \tag{C4}$$

Divide Eqs. (C3) and (C4) by Δz, taking the limit as $\Delta z \to 0$, and rearranging

$$\frac{d\dot{m}_F}{dz} = -N_{fibers} 2\pi R_o B_{MD} \left(P_F^{Sat} - P_D^{Sat} \right) \tag{C5}$$

$$\frac{d\dot{m}_D}{dz} = -N_{fibers} 2\pi R_o B_{MD} \left(P_F^{Sat} - P_D^{Sat} \right) \tag{C6}$$

Energy balance on feed and distillate side

$$\dot{m}_F(z) c_p T_F(z) - \dot{m}_F(z+\Delta z) c_p T_F(z+\Delta z) - U N_{fibers} 2\pi R_o \Delta z \left(T_F(z) - T_D(z) \right) = 0 \tag{C7}$$

$$\dot{m}_D\left(z+\Delta z\right)c_pT_D\left(z+\Delta z\right)-\dot{m}_D\left(z\right)c_pT_D\left(z\right)+UN_{fibers}2\pi R_o\Delta z\left(T_F\left(z\right)-T_D\left(z\right)\right)=0 \quad \text{(C8)}$$

Divide (C7) and (C8) by Δz, taking the limit as Δz → 0, and rearranging

$$c_p\left[\frac{d\dot{m}_F}{dz}T_F\left(z\right)+\frac{dT_F}{dz}\dot{m}_F\left(z\right)\right]+UN_{fibers}2\pi R_o\left(T_F\left(z\right)-T_D\left(z\right)\right)=0 \quad \text{(C9)}$$

$$c_p\left[\frac{d\dot{m}_D}{dz}T_D\left(z\right)+\frac{dT_D}{dz}\dot{m}_D\left(z\right)\right]+UN_{fibers}2\pi R_o\left(T_F\left(z\right)-T_D\left(z\right)\right)=0 \quad \text{(C10)}$$

Solve Eqs. (C9) and (C10) for dT_F/dz and dT_D/dz using Eqs. (C5) and (C6)

$$\frac{dT_F}{dz}=\frac{-UN_{fibers}2\pi R_o\left(T_F\left(z\right)-T_D\left(z\right)\right)+N_{fibers}2\pi R_oB_{MD}\left(P_F^{Sat}-P_D^{Sat}\right)c_pT_F\left(z\right)}{c_p\dot{m}_F\left(z\right)} \quad \text{(C11)}$$

$$\frac{dT_D}{dz}=\frac{-UN_{fibers}2\pi R_o\left(T_F\left(z\right)-T_D\left(z\right)\right)+N_{fibers}2\pi R_oB_{MD}\left(P_F^{Sat}-P_D^{Sat}\right)c_pT_D\left(z\right)}{c_p\dot{m}_D\left(z\right)} \quad \text{(C12)}$$

Equations (C5), (C6), (C11), and (C12) are governing ODEs that describe the heat and mass transfer in hollow fiber module for DCMD. The boundary conditions (BCs) for counter current DCMD would be:

$$\dot{m}_F\left(0\right)=\dot{m}_{F,in}; \ \dot{m}_D(L)=\dot{m}_{D,in}; \ T_F\left(0\right)=T_{F,in};T_D(L)=T_{D,in}$$

Where L is the length of the module. The same analysis for cocurrent DCMD yields:

$$\frac{d\dot{m}_F}{dz}=-N_{fibers}2\pi R_oB_{MD}\left(P_F^{Sat}-P_D^{Sat}\right) \quad \text{(C13)}$$

$$\frac{d\dot{m}_D}{dz}=N_{fibers}2\pi R_oB_{MD}\left(P_F^{Sat}-P_D^{Sat}\right) \quad \text{(C14)}$$

$$\frac{dT_F}{dz} = \frac{-U N_{fibers} 2\pi R_o \left(T_F\left(z\right) - T_D\left(z\right)\right) + N_{fibers} 2\pi R_o B_{MD} \left(P_F^{Sat} - P_D^{Sat}\right) c_p T_F\left(z\right)}{c_p \dot{m}_F\left(z\right)} \tag{C15}$$

$$\frac{dT_D}{dz} = \frac{U N_{fibers} 2\pi R_o \left(T_F\left(z\right) - T_D\left(z\right)\right) - N_{fibers} 2\pi R_o B_{MD} \left(P_F^{Sat} - P_D^{Sat}\right) c_p T_D\left(z\right)}{c_p \dot{m}_D\left(z\right)} \tag{C16}$$

With BCs:

$$\dot{m}_F(0) = \dot{m}_{F,in} \, ; \ \dot{m}_D(0) = \dot{m}_{D,in} \, ; \ \ T_F(0) = T_{F,in} \, ; T_D(0) = T_{D,in}$$

Nomenclature and Abbreviation

Nomenclature

A_m Area of membrane

B_g Gas permeability (Eq. (3.4))

B_{MD} Membrane distillation mass transfer coefficient

C Concentration

c_p Specific heat capacity

d_p Pore diameter (or size)

g Specific Gibbs free energy

J Water flux

J_0 Initial water flux

J_g Gas flux

k Boltzmann's constant

$\dot{m}$ Mass flow rate

n Number of molecules or segments (Eq (2.3))

N_{fibers} Number of fibers

P^{Sat} Vapor pressure

$\dot{Q}$ Heat transfer rate

$\dot{Q}_S$ Incoming solar power

R	Salt rejection or gas constant
Ra	Solubility parameter distance
R_o	Interaction radius of the solubility parameter or outer radius of hollow fiber
S	Entropy
$\dot{S}_{gen}$	Entropy generation rate
T	Temperature
t	Time
T_0	Dead state temperature of the environment
T_S	Apparent temperature of the sun as an energy source [112]
v	Molar volume
V	Volume
z	Axial position
ΔG_m	Gibbs free energy of mixing
ΔP	Differential pressure difference
χ_{12}	Flory interaction parameter
δ	Solubility parameter
ϕ	Volume fraction
γ	Surface tension

ζ_{gen}	Specific entropy generation
φ	Packing density
θ	Contact angle
ρ	Density

Abbreviations

AGMD	Air gap membrane distillation
D	Distillate
DCMD	Direct contact membrane distillate
ED	Electrodialysis
F	Feed
FO	Forward osmosis
HX	Heat exchanger
I.D.	Inner diameter
IPA	Isopropyl alcohol
LEP	Liquid entry pressure
MD	Membrane distillation
MED	Multi-effect distillation
MSF	Multi-stage flash

O.D.	Outer diameter
ODE	Ordinary differential equation
PBSF	Perfluorobutanesulfonyl fluoride
PP	Polypropylene
pPFDA	Poly (1H,1H,2H,2H-perfluorodecyl acrylate)
PTFE	Polytetrafluoroethylene
PVDF	Polyvinylidene fluoride
REM	Relative energy difference
RO	Reverse osmosis
SC	Solar collector
SDS	Sodium dodecyl sulfate
SEM	Scanning electron microscopy
SGMD	Sweeping gas membrane distillation
TEP	Triethyl phosphate
VMD	Vacuum membrane distillation

References

[1] World Water Development Report 2019, Paris, 2019. https://www.unwater.org/publications/world-water-development-report-2019/ (accessed June 25, 2019).

[2] Drinking-water, (2019). https://www.who.int/news-room/fact-sheets/detail/drinking-water (accessed June 25, 2019).

[3] Where is Earth's Water?, (n.d.). https://www.usgs.gov/special-topic/water-science-school/science/where-earths-water?qt-science_center_objects=0#qt-science_center_objects (accessed July 21, 2019).

[4] K. Scott, Can the Middle East solve its water problem?, CNN. (2019). https://www.cnn.com/2018/07/11/middleeast/middle-east-water/index.html (accessed July 30, 2019).

[5] S. KALOGIROU, Seawater desalination using renewable energy sources, Prog. Energy Combust. Sci. 31 (2005) 242–281. doi:10.1016/j.pecs.2005.03.001.

[6] M. Elimelech, W.A. Phillip, The Future of Seawater Desalination: Energy, Technology, and the Environment, Science (80-.). 333 (2011) 712–717. doi:10.1126/science.1200488.

[7] E. Jones, M. Qadir, M.T.H. van Vliet, V. Smakhtin, S. Kang, The state of desalination and brine production: A global outlook, Sci. Total Environ. 657 (2019) 1343–1356. doi:10.1016/j.scitotenv.2018.12.076.

[8] P.K. Cornejo, M.V.E. Santana, D.R. Hokanson, J.R. Mihelcic, Q. Zhang, Carbon footprint of water reuse and desalination: a review of greenhouse gas emissions and estimation tools, J. Water Reuse Desalin. 4 (2014) 238–252. doi:10.2166/wrd.2014.058.

[9] R.G. Raluy, L. Serra, J. Uche, A. Valero, Life-cycle assessment of desalination technologies integrated with energy production systems, Desalination. 167 (2004) 445–458. doi:10.1016/j.desal.2004.06.160.

[10] R. Semiat, Energy Issues in Desalination Processes, Environ. Sci. Technol. 42 (2008) 8193–8201. doi:10.1021/es801330u.

[11] RENEWABLE POWER GENERATION COSTS IN 2018, Abu Dhabi, 2019. www.irena.org (accessed July 12, 2019).

[12] R. Fu, D. Feldman, R. Margolis, U.S. Solar Photovoltaic System Cost Benchmark: Q1 2018, Golden, CO, 2018. https://www.nrel.gov/docs/fy19osti/72399.pdf (accessed April 16, 2019).

[13] M.T. Ali, H.E.S. Fath, P.R. Armstrong, A comprehensive techno-economical review of indirect solar desalination, Renew. Sustain. Energy Rev. 15 (2011) 4187–4199. doi:10.1016/j.rser.2011.05.012.

[14] A.J. Hughes, T.S. O'Donovan, T.K. Mallick, Experimental Evaluation of a

Membrane Distillation System for Integration with Concentrated Photovoltaic/Thermal (CPV/T) Energy, Energy Procedia. 54 (2014) 725–733. doi:10.1016/j.egypro.2014.07.313.

[15] X. Wang, L. Zhang, H. Yang, H. Chen, Feasibility research of potable water production via solar-heated hollow fiber membrane distillation system, Desalination. 247 (2009) 403–411. doi:10.1016/j.desal.2008.10.008.

[16] J.-P. Mericq, S. Laborie, C. Cabassud, Evaluation of systems coupling vacuum membrane distillation and solar energy for seawater desalination, Chem. Eng. J. 166 (2011) 596–606. doi:10.1016/j.cej.2010.11.030.

[17] H. Chang, S.-G. Lyu, C.-M. Tsai, Y.-H. Chen, T.-W. Cheng, Y.-H. Chou, Experimental and simulation study of a solar thermal driven membrane distillation desalination process, Desalination. 286 (2012) 400–411. doi:10.1016/j.desal.2011.11.057.

[18] R.G. Raluy, R. Schwantes, V.J. Subiela, B. Peñate, G. Melián, J.R. Betancort, Operational experience of a solar membrane distillation demonstration plant in Pozo Izquierdo-Gran Canaria Island (Spain), Desalination. 290 (2012) 1–13. doi:10.1016/j.desal.2012.01.003.

[19] F. Banat, N. Jwaied, M. Rommel, J. Koschikowski, M. Wieghaus, Performance evaluation of the "large SMADES" autonomous desalination solar-driven membrane distillation plant in Aqaba, Jordan, Desalination. 217 (2007) 17–28. doi:10.1016/j.desal.2006.11.027.

[20] A. Deshmukh, C. Boo, V. Karanikola, S. Lin, A.P. Straub, T. Tong, D.M. Warsinger, M. Elimelech, Membrane distillation at the water-energy nexus: limits, opportunities, and challenges, Energy Environ. Sci. 11 (2018) 1177–1196. doi:10.1039/C8EE00291F.

[21] C. Boo, J. Lee, M. Elimelech, Omniphobic Polyvinylidene Fluoride (PVDF) Membrane for Desalination of Shale Gas Produced Water by Membrane Distillation, Environ. Sci. Technol. 50 (2016) 12275–12282. doi:10.1021/acs.est.6b03882.

[22] C.R. Martinetti, A.E. Childress, T.Y. Cath, High recovery of concentrated RO brines using forward osmosis and membrane distillation, J. Memb. Sci. 331 (2009) 31–39. doi:10.1016/j.memsci.2009.01.003.

[23] M. Laqbaqbi, M.C. García-Payo, M. Khayet, J. El Kharraz, M. Chaouch, Application of direct contact membrane distillation for textile wastewater treatment and fouling study, Sep. Purif. Technol. 209 (2019) 815–825. doi:10.1016/j.seppur.2018.09.031.

[24] M. Gryta, The Application of Membrane Distillation for Broth Separation in Membrane Bioreactors, J. Membr. Sci. Res. 2 (2016) 193–200. doi:10.22079/JMSR.2016.21950.

[25] V. Karanikola, C. Boo, J. Rolf, M. Elimelech, Engineered Slippery Surface to

Mitigate Gypsum Scaling in Membrane Distillation for Treatment of Hypersaline Industrial Wastewaters, Environ. Sci. Technol. 52 (2018) 14362–14370. doi:10.1021/acs.est.8b04836.

[26] M.R. Choudhury, N. Anwar, D. Jassby, M.S. Rahaman, Fouling and wetting in the membrane distillation driven wastewater reclamation process – A review, Adv. Colloid Interface Sci. 269 (2019) 370–399. doi:10.1016/j.cis.2019.04.008.

[27] D.L. Shaffer, L.H. Arias Chavez, M. Ben-Sasson, S. Romero-Vargas Castrillón, N.Y. Yip, M. Elimelech, Desalination and Reuse of High-Salinity Shale Gas Produced Water: Drivers, Technologies, and Future Directions, Environ. Sci. Technol. 47 (2013) 9569–9583. doi:10.1021/es401966e.

[28] M. Khayet, Solar desalination by membrane distillation: Dispersion in energy consumption analysis and water production costs (a review), Desalination. 308 (2013) 89–101. doi:10.1016/j.desal.2012.07.010.

[29] N. Thomas, M.O. Mavukkandy, S. Loutatidou, H.A. Arafat, Membrane distillation research & implementation: Lessons from the past five decades, Sep. Purif. Technol. 189 (2017) 108–127. doi:10.1016/j.seppur.2017.07.069.

[30] M. Khayet, T. Matsuura, Membrane Distillation, Elsevier, Amsterdam, The Netherlands, 2011. doi:10.1016/C2009-0-17487-1.

[31] C.-Y. Kuo, H.-N. Lin, H.-A. Tsai, D.-M. Wang, J.-Y. Lai, Fabrication of a high hydrophobic PVDF membrane via nonsolvent induced phase separation, Desalination. 233 (2008) 40–47. doi:10.1016/j.desal.2007.09.025.

[32] S. Bonyadi, T.-S. Chung, Highly porous and macrovoid-free PVDF hollow fiber membranes for membrane distillation by a solvent-dope solution co-extrusion approach, J. Memb. Sci. 331 (2009) 66–74. doi:10.1016/j.memsci.2009.01.014.

[33] S. Bonyadi, T.S. Chung, Flux enhancement in membrane distillation by fabrication of dual layer hydrophilic–hydrophobic hollow fiber membranes, J. Memb. Sci. 306 (2007) 134–146. doi:10.1016/j.memsci.2007.08.034.

[34] Y. Liu, T. Xiao, C. Bao, Y. Fu, X. Yang, Fabrication of novel Janus membrane by nonsolvent thermally induced phase separation (NTIPS) for enhanced performance in membrane distillation, J. Memb. Sci. 563 (2018) 298–308. doi:10.1016/j.memsci.2018.05.067.

[35] S. Lin, S. Nejati, C. Boo, Y. Hu, C.O. Osuji, M. Elimelech, Omniphobic Membrane for Robust Membrane Distillation, Environ. Sci. Technol. Lett. 1 (2014) 443–447. doi:10.1021/ez500267p.

[36] M. Gryta, Long-term performance of membrane distillation process, J. Memb. Sci. 265 (2005) 153–159. doi:10.1016/j.memsci.2005.04.049.

[37] M. Gryta, Fouling in direct contact membrane distillation process, J. Memb. Sci. 325 (2008) 383–394. doi:10.1016/j.memsci.2008.08.001.

[38] N.G.P. Chew, S. Zhao, C.H. Loh, N. Permogorov, R. Wang, Surfactant effects on

water recovery from produced water via direct-contact membrane distillation, J. Memb. Sci. 528 (2017) 126–134. doi:10.1016/j.memsci.2017.01.024.

[39] M. GRYTA, Influence of polypropylene membrane surface porosity on the performance of membrane distillation process, J. Memb. Sci. 287 (2007) 67–78. doi:10.1016/j.memsci.2006.10.011.

[40] M. Rezaei, D.M. Warsinger, J.H. Lienhard V, M.C. Duke, T. Matsuura, W.M. Samhaber, Wetting phenomena in membrane distillation: Mechanisms, reversal, and prevention, Water Res. 139 (2018) 329–352. doi:10.1016/j.watres.2018.03.058.

[41] M. Qtaishat, T. Matsuura, B. Kruczek, M. Khayet, Heat and mass transfer analysis in direct contact membrane distillation, Desalination. 219 (2008) 272–292. doi:10.1016/j.desal.2007.05.019.

[42] D.M. Warsinger, J. Swaminathan, E. Guillen-Burrieza, H.A. Arafat, J.H. Lienhard V, Scaling and fouling in membrane distillation for desalination applications: A review, Desalination. 356 (2015) 294–313. doi:10.1016/j.desal.2014.06.031.

[43] Z. Wang, D. Hou, S. Lin, Composite Membrane with Underwater-Oleophobic Surface for Anti-Oil-Fouling Membrane Distillation, Environ. Sci. Technol. 50 (2016) 3866–3874. doi:10.1021/acs.est.5b05976.

[44] Y.-X. Huang, Z. Wang, J. Jin, S. Lin, Novel Janus Membrane for Membrane Distillation with Simultaneous Fouling and Wetting Resistance, Environ. Sci. Technol. 51 (2017) 13304–13310. doi:10.1021/acs.est.7b02848.

[45] Z. Zhu, Z. Liu, L. Zhong, C. Song, W. Shi, F. Cui, W. Wang, Breathable and asymmetrically superwettable Janus membrane with robust oil-fouling resistance for durable membrane distillation, J. Memb. Sci. 563 (2018) 602–609. doi:10.1016/j.memsci.2018.06.028.

[46] G. Zuo, R. Wang, Novel membrane surface modification to enhance anti-oil fouling property for membrane distillation application, J. Memb. Sci. 447 (2013) 26–35. doi:10.1016/j.memsci.2013.06.053.

[47] D. Hou, C. Ding, K. Li, D. Lin, D. Wang, J. Wang, A novel dual-layer composite membrane with underwater-superoleophobic/hydrophobic asymmetric wettability for robust oil-fouling resistance in membrane distillation desalination, Desalination. 428 (2018) 240–249. doi:10.1016/j.desal.2017.11.039.

[48] Z. Wang, S. Lin, Membrane fouling and wetting in membrane distillation and their mitigation by novel membranes with special wettability, Water Res. 112 (2017) 38–47. doi:10.1016/J.WATRES.2017.01.022.

[49] Z. Wang, S. Lin, The impact of low-surface-energy functional groups on oil fouling resistance in membrane distillation, J. Memb. Sci. 527 (2017) 68–77. doi:10.1016/J.MEMSCI.2016.12.063.

[50] F. He, K.K. Sirkar, J. Gilron, Effects of antiscalants to mitigate membrane scaling by direct contact membrane distillation, J. Memb. Sci. 345 (2009) 53–58. doi:10.1016/J.MEMSCI.2009.08.021.

[51] M. Gryta, The assessment of microorganism growth in the membrane distillation system, Desalination. 142 (2002) 79–88. doi:10.1016/S0011-9164(01)00427-1.

[52] M. Krivorot, A. Kushmaro, Y. Oren, J. Gilron, Factors affecting biofilm formation and biofouling in membrane distillation of seawater, J. Memb. Sci. 376 (2011) 15–24. doi:10.1016/j.memsci.2011.01.061.

[53] M. Mohammadi Ghaleni, A. Al Balushi, S. Kaviani, E. Tavakoli, M. Bavarian, S. Nejati, Fabrication of Janus Membranes for Desalination of Oil-Contaminated Saline Water, ACS Appl. Mater. Interfaces. 10 (2018) 44871–44879. doi:10.1021/acsami.8b16621.

[54] R. Zheng, Y. Chen, J. Wang, J. Song, X.-M. Li, T. He, Preparation of omniphobic PVDF membrane with hierarchical structure for treating saline oily wastewater using direct contact membrane distillation, J. Memb. Sci. 555 (2018) 197–205. doi:10.1016/J.MEMSCI.2018.03.041.

[55] Y.C. Woo, Y. Kim, M. Yao, L.D. Tijing, J.-S. Choi, S. Lee, S.-H. Kim, H.K. Shon, Hierarchical Composite Membranes with Robust Omniphobic Surface Using Layer-By-Layer Assembly Technique, Environ. Sci. Technol. 52 (2018) 2186–2196. doi:10.1021/acs.est.7b05450.

[56] L.-H. Chen, A. Huang, Y.-R. Chen, C.-H. Chen, C.-C. Hsu, F.-Y. Tsai, K.-L. Tung, Omniphobic membranes for direct contact membrane distillation: Effective deposition of zinc oxide nanoparticles, Desalination. 428 (2018) 255–263. doi:10.1016/J.DESAL.2017.11.029.

[57] K.J. Lu, J. Zuo, J. Chang, H.N. Kuan, T.-S. Chung, Omniphobic Hollow-Fiber Membranes for Vacuum Membrane Distillation, Environ. Sci. Technol. 52 (2018) 4472–4480. doi:10.1021/acs.est.8b00766.

[58] C. Lu, C. Su, H. Cao, X. Ma, F. Duan, J. Chang, Y. Li, F-POSS based Omniphobic Membrane for Robust Membrane Distillation, Mater. Lett. 228 (2018) 85–88. doi:10.1016/J.MATLET.2018.05.126.

[59] E. Torres-Reyes, J.. Cervantes-de Gortari, B.. Ibarra-Salazar, M. Picon-Nuñez, A design method of flat-plate solar collectors based on minimum entropy generation, Exergy, An Int. J. 1 (2001) 46–52. doi:10.1016/S1164-0235(01)00009-7.

[60] H. Zhang, R. Lamb, J. Lewis, Engineering nanoscale roughness on hydrophobic surface - Preliminary assessment of fouling behaviour, Sci. Technol. Adv. Mater. 6 (2005) 236–239. doi:10.1016/j.stam.2005.03.003.

[61] Y. Liao, R. Wang, A.G. Fane, Engineering superhydrophobic surface on poly(vinylidene fluoride) nanofiber membranes for direct contact membrane distillation, J. Memb. Sci. 440 (2013) 77–87. doi:10.1016/j.memsci.2013.04.006.

[62] S. Li, Q. Jiang, S. Liu, Y. Zhang, Y. Tian, C. Song, J. Wang, Y. Zou, G.J. Anderson, J.-Y. Han, Y. Chang, Y. Liu, C. Zhang, L. Chen, G. Zhou, G. Nie, H. Yan, B. Ding, Y. Zhao, A DNA nanorobot functions as a cancer therapeutic in response to a molecular trigger in vivo, Nat. Biotechnol. 36 (2018) 258–264.

doi:10.1038/nbt.4071.

[63] H.-W. Liang, X. Cao, F. Zhou, C.-H. Cui, W.-J. Zhang, S.-H. Yu, A Free-Standing Pt-Nanowire Membrane as a Highly Stable Electrocatalyst for the Oxygen Reduction Reaction, Adv. Mater. 23 (2011) 1467–1471. doi:10.1002/adma.201004377.

[64] D. Proctor, A generalized method for testing all classes of solar collector—II evaluation of collector thermal constants, Sol. Energy. 32 (1984) 377–386. doi:10.1016/0038-092X(84)90282-2.

[65] D. Proctor, A generalized method for testing all classes of solar collector—III linearized efficiency equations, Sol. Energy. 32 (1984) 377–386. doi:10.1016/0038-092X(84)90282-2.

[66] A.E. Childress, P. Le-Clech, J.L. Daugherty, C. Chen, G.L. Leslie, Mechanical analysis of hollow fiber membrane integrity in water reuse applications, Desalination. 180 (2005) 5–14. doi:10.1016/J.DESAL.2004.12.026.

[67] F. Liu, N.A. Hashim, Y. Liu, M.R.M. Abed, K. Li, Progress in the production and modification of PVDF membranes, J. Memb. Sci. 375 (2011) 1–27. doi:10.1016/J.MEMSCI.2011.03.014.

[68] H. Strathmann, K. Kock, P. Amar, R.W. Baker, The formation mechanism of asymmetric membranes, Desalination. 16 (1975) 179–203. doi:10.1016/S0011-9164(00)82092-5.

[69] C. Boo, J. Lee, M. Elimelech, Engineering Surface Energy and Nanostructure of Microporous Films for Expanded Membrane Distillation Applications, Environ. Sci. Technol. 50 (2016) 8112–8119. doi:10.1021/acs.est.6b02316.

[70] A. Alkhudhiri, N. Darwish, N. Hilal, Membrane distillation: A comprehensive review, Desalination. 287 (2012) 2–18. doi:10.1016/J.DESAL.2011.08.027.

[71] M.S. El-Bourawi, Z. Ding, R. Ma, M. Khayet, A framework for better understanding membrane distillation separation process, J. Memb. Sci. 285 (2006) 4–29. doi:10.1016/j.memsci.2006.08.002.

[72] G. dong Kang, Y. ming Cao, Application and modification of poly(vinylidene fluoride) (PVDF) membranes - A review, J. Memb. Sci. 463 (2014) 145–165. doi:10.1016/j.memsci.2014.03.055.

[73] F.Y.C. Huang, A. Arning, Performance Comparison between Polyvinylidene Fluoride and Polytetrafluoroethylene Hollow Fiber Membranes for Direct Contact Membrane Distillation, Membranes (Basel). 9 (2019) 52. doi:10.3390/membranes9040052.

[74] E. Drioli, A. Ali, S. Simone, F. Macedonio, S.A. AL-Jlil, F.S. Al Shabonah, H.S. Al-Romaih, O. Al-Harbi, A. Figoli, A. Criscuoli, Novel PVDF hollow fiber membranes for vacuum and direct contact membrane distillation applications, Sep. Purif. Technol. 115 (2013) 27–38. doi:10.1016/j.seppur.2013.04.040.

[75] K. Yu Wang, T.-S. Chung, M. Gryta, Hydrophobic PVDF hollow fiber membranes with narrow pore size distribution and ultra-thin skin for the fresh water production through membrane distillation, Chem. Eng. Sci. 63 (2008) 2587–2594. doi:10.1016/j.ces.2008.02.020.

[76] J. Chang, J. Zuo, L. Zhang, G.S. O'Brien, T.-S. Chung, Using green solvent, triethyl phosphate (TEP), to fabricate highly porous PVDF hollow fiber membranes for membrane distillation, J. Memb. Sci. 539 (2017) 295–304. doi:10.1016/j.memsci.2017.06.002.

[77] H. Matsuyama, S. Rajabzadeh, H. Karkhanechi, S. Jeon, 1.7 PVDF Hollow Fibers Membranes, in: Compr. Membr. Sci. Eng., Elsevier, 2017: pp. 137–189. doi:10.1016/B978-0-12-409547-2.12244-9.

[78] G.R. Guillen, Y. Pan, M. Li, E.M. V. Hoek, Preparation and Characterization of Membranes Formed by Nonsolvent Induced Phase Separation: A Review, Ind. Eng. Chem. Res. 50 (2011) 3798–3817. doi:10.1021/ie101928r.

[79] Z. Chen, D. Rana, T. Matsuura, D. Meng, C.Q. Lan, Study on structure and vacuum membrane distillation performance of PVDF membranes: II. Influence of molecular weight, Chem. Eng. J. 276 (2015) 174–184. doi:10.1016/J.CEJ.2015.04.030.

[80] S. Nejati, C. Boo, C.O. Osuji, M. Elimelech, Engineering flat sheet microporous PVDF films for membrane distillation, J. Memb. Sci. 492 (2015) 355–363. doi:10.1016/j.memsci.2015.05.033.

[81] A.K. Hołda, I.F.J. Vankelecom, Understanding and guiding the phase inversion process for synthesis of solvent resistant nanofiltration membranes, J. Appl. Polym. Sci. 132 (2015) n/a-n/a. doi:10.1002/app.42130.

[82] A. Figoli, T. Marino, S. Simone, E. Di Nicolò, X.-M. Li, T. He, S. Tornaghi, E. Drioli, Towards non-toxic solvents for membrane preparation: a review, Green Chem. 16 (2014) 4034. doi:10.1039/C4GC00613E.

[83] C.M. Hansen, Hansen Solubility Parameters: A User's Handbook, Second, CRC Press, Roca Raton, FL, 2007. https://www.crcpress.com/Hansen-Solubility-Parameters-A-Users-Handbook-Second-Edition/Hansen/p/book/9780849372483.

[84] J.M. Prausnitz, R.N. Lichtenthaler, E.G. de Azevendo, Molecular Thermodynamics of Fluid-Phase Equilibria, 3rd ed., Prentice Hall, Upper Saddle River, NJ, 1999.

[85] R. Koningsveld, L.A. Kleintjens, H.M. Schoffeleers, Thermodynamic aspects of polymer compatibility, Pure Appl. Chem. 39 (1974) 1–32. doi:10.1351/pac197439010001.

[86] H. Strathmann, K. Kock, The formation mechanism of phase inversion membranes, Desalination. 21 (1977) 241–255. doi:10.1016/S0011-9164(00)88244-2.

[87] M. Haponska, A. Trojanowska, A. Nogalska, R. Jastrzab, T. Gumi, B. Tylkowski, PVDF Membrane Morphology—Influence of Polymer Molecular Weight and Preparation Temperature, Polymers (Basel). 9 (2017) 718. doi:10.3390/polym9120718.

[88] S.P. Deshmukh, K. Li, Effect of ethanol composition in water coagulation bath on morphology of PVDF hollow fibre membranes, J. Memb. Sci. 150 (1998) 75–85. doi:10.1016/S0376-7388(98)00196-3.

[89] W.E. Tenhaeff, K.K. Gleason, Initiated and Oxidative Chemical Vapor Deposition of Polymeric Thin Films: iCVD and oCVD, Adv. Funct. Mater. 18 (2008) 979–992. doi:10.1002/adfm.200701479.

[90] POROLUX^{TM} Pressure Step/Stability Series, n.d. https://particulatesystems.com/wp-content/uploads/2019/02/POROMETER2018-Particulate-Systems.pdf (accessed June 27, 2019).

[91] A.T. Servi, E. Guillen-Burrieza, D.M. Warsinger, W. Livernois, K. Notarangelo, J. Kharraz, J.H. Lienhard V, H.A. Arafat, K.K. Gleason, The effects of iCVD film thickness and conformality on the permeability and wetting of MD membranes, J. Memb. Sci. 523 (2017) 470–479. doi:10.1016/J.MEMSCI.2016.10.008.

[92] M. Khayet, A. Velázquez, J.I. Mengual, Modelling mass transport through a porous partition: Effect of pore size distribution, J. Non-Equilibrium Thermodyn. 29 (2004) 279–299. doi:10.1515/JNETDY.2004.055.

[93] X. Feng, L. Jiang, Design and creation of superwetting/antiwetting surfaces, Adv. Mater. 18 (2006) 3063–3078. doi:10.1002/adma.200501961.

[94] R. Nazari Moghaddam, M. Jamiolahmady, Slip flow in porous media, Fuel. 173 (2016) 298–310. doi:10.1016/j.fuel.2016.01.057.

[95] J. Kong, K. Li, An improved gas permeation method for characterising and predicting the performance of microporous asymmetric hollow fibre membranes used in gas absorption, J. Memb. Sci. 182 (2001) 271–281. doi:10.1016/S0376-7388(00)00573-1.

[96] A.T. Servi, J. Kharraz, D. Klee, K. Notarangelo, B. Eyob, E. Guillen-Burrieza, A. Liu, H.A. Arafat, K.K. Gleason, A systematic study of the impact of hydrophobicity on the wetting of MD membranes, J. Memb. Sci. 520 (2016) 850–859. doi:10.1016/J.MEMSCI.2016.08.021.

[97] F. Guo, A. Servi, A. Liu, K.K. Gleason, G.C. Rutledge, Desalination by membrane distillation using electrospun polyamide fiber membranes with surface fluorination by chemical vapor deposition, ACS Appl. Mater. Interfaces. 7 (2015) 8225–8232. doi:10.1021/acsami.5b01197.

[98] M. Mohammadi Ghaleni, M. Bavarian, S. Nejati, Model-guided design of high-performance membrane distillation modules for water desalination, J. Memb. Sci. 563 (2018) 794–803. doi:10.1016/J.MEMSCI.2018.06.054.

[99] S. Al-Obaidani, E. Curcio, F. Macedonio, G. Di Profio, H. Al-Hinai, E. Drioli, Potential of membrane distillation in seawater desalination: Thermal efficiency, sensitivity study and cost estimation, J. Memb. Sci. 323 (2008) 85–98. doi:10.1016/J.MEMSCI.2008.06.006.

[100] M.M. Teoh, S. Bonyadi, T.-S. Chung, Investigation of different hollow fiber module

designs for flux enhancement in the membrane distillation process, J. Memb. Sci. 311 (2008) 371–379. doi:10.1016/J.MEMSCI.2007.12.054.

[101] E. Matijević, B.A. Pethica, The properties of ionized monolayers. Part 1.—Sodium dodecyl sulphate at the air/water interface, Trans. Faraday Soc. 54 (1958) 1382–1389. doi:10.1039/TF9585401382.

[102] Z. Wang, Y. Chen, S. Lin, Kinetic model for surfactant-induced pore wetting in membrane distillation, J. Memb. Sci. 564 (2018) 275–288. doi:10.1016/J.MEMSCI.2018.07.010.

[103] A. Fakhru'l-Razi, A. Pendashteh, L.C. Abdullah, D.R.A. Biak, S.S. Madaeni, Z.Z. Abidin, Review of technologies for oil and gas produced water treatment, J. Hazard. Mater. 170 (2009) 530–551. doi:10.1016/J.JHAZMAT.2009.05.044.

[104] R.N. Wenzel, RESISTANCE OF SOLID SURFACES TO WETTING BY WATER, Ind. Eng. Chem. 28 (1936) 988–994. doi:10.1021/ie50320a024.

[105] A.B.D. Cassie, S. Baxter, Wettability of porous surfaces, Trans. Faraday Soc. 40 (1944) 546. doi:10.1039/tf9444000546.

[106] J. Yang, H. Song, X. Yan, H. Tang, C. Li, Superhydrophilic and superoleophobic chitosan-based nanocomposite coatings for oil/water separation, Cellulose. 21 (2014) 1851–1857. doi:10.1007/s10570-014-0244-0.

[107] P.-J. Lin, M.-C. Yang, Y.-L. Li, J.-H. Chen, Prevention of surfactant wetting with agarose hydrogel layer for direct contact membrane distillation used in dyeing wastewater treatment, J. Memb. Sci. 475 (2015) 511–520. doi:10.1016/J.MEMSCI.2014.11.001.

[108] K.H. Mistry, R.K. McGovern, G.P. Thiel, E.K. Summers, S.M. Zubair, J.H. Lienhard, Entropy Generation Analysis of Desalination Technologies, Entropy. 13 (2011) 1829–1864. doi:10.3390/e13101829.

[109] S. Lin, N.Y. Yip, M. Elimelech, Direct contact membrane distillation with heat recovery: Thermodynamic insights from module scale modeling, J. Memb. Sci. 453 (2014) 498–515. doi:10.1016/J.MEMSCI.2013.11.016.

[110] A. Deshmukh, M. Elimelech, Understanding the impact of membrane properties and transport phenomena on the energetic performance of membrane distillation desalination, J. Memb. Sci. 539 (2017) 458–474. doi:10.1016/j.memsci.2017.05.017.

[111] A.G. Fane, R.W. Schofield, C.J.D. Fell, The efficient use of energy in membrane distillation, Desalination. 64 (1987) 231–243. doi:10.1016/0011-9164(87)90099-3.

[112] A. Bejan, D.W. Kearney, F. Kreith, Second Law Analysis and Synthesis of Solar Collector Systems, J. Sol. Energy Eng. 103 (1981) 23. doi:10.1115/1.3266200.

[113] J.H. Lienhard, K.H. Mistry, M.H. Sharqawy, G.P. Thiel, Thermodynamics, Exergy, and Energy Efficiency in Desalination Systems, in: Desalin. Sustain., Elsevier, 2017: pp. 127–206. doi:10.1016/B978-0-12-809791-5.00004-3.

[114] D. Warsinger, K. Mistry, K. Nayar, H. Chung, J. Lienhard V, Entropy Generation of Desalination Powered by Variable Temperature Waste Heat, Entropy. 17 (2015) 7530–7566. doi:10.3390/e17117530.

[115] K. Mistry, J. Lienhard, Generalized Least Energy of Separation for Desalination and Other Chemical Separation Processes, Entropy. 15 (2013) 2046–2080. doi:10.3390/e15062046.